UNIVERSITY OF POTSDAM

Institute of Earth- and Environmental Science

Short-term changes of permafrost degradation triggered by anthropogenic impacts and climatic events in Western Siberia 2010-2013

MASTER THESIS

to attain the academic degree
Master of Science (M.Sc.) in Geoscience

Submitted by

Caroline Noerling

Berlin, April 2017

Caroline Noerling

Student number: 750936

Email: noerling@uni-potsdam,de

Supervisors	**Dr. Anne Morgenstern**	**apl. Prof. Dr. Bernhard Diekmann**
Address	Alfred-Wegener-Institute Telegrafenberg A43 D-14473 Potsdam	Alfred-Wegener-Institute Telegrafenberg A43 D-14473 Potsdam
Email	Anne.Morgenstern@awi.de	Bernhard.Diekmann@awi.de

Content

List of Figures

List of Tables

List of Abbreviations

ALD	Active Layer Detachments
ALT	Active Layer Thickness
ASCAT	Advanced SCATerometer
a.s.l.	above sea level
°C	Celsius
cm	centimeter
DEM	Digital Elevation Model
E	East
ECMWF	European Centre for Medium-Range Weather Forecast
e.g.	Latin: exempli gratia; for example
FI	Freezing Index
km	kilometer
km^2	square kilometer
m	meter
mm	millimeter
m^3	cubic meter
n	number
N	North
NDVI	Normalized Difference Vegetation Index
NIR	Near Infrared
NetCDF	Network Common Data Format
NOAA	National Oceanic and Atmospheric Administration
Pg	Pentagram
r	Pearson Coefficient
RMS	Root Mean Square
RTS	Retrogressive Thaw Slumps
S	South
SSF	Surface State Flag
TI	Thawing Index
UTC	Universal Transverse Mercator
W	West
WGS	World Geodetic System

Abstract

In light of climate warming, ice-rich permafrost landscapes are amongst the most vulnerable areas in the world. In addition, many regions in the Arctic are affected by rapid industrial development as natural resources become more and more accessible through transportation networks and new engineering technologies. The aim of this study is to examine short-term anthropogenic and natural disturbances on permafrost, in particular whether there is a relation between the effects of infrastructure and the occurrence of landslides.

The study investigates a region in Central Yamal, NW Siberia, that was affected by the construction of the Bovanenkovo railway line and by high Retrogressive Thaw Slumps (RTS) occurrence in consequence of the extremely warm and wet year 2012. A change detection was performed using high optical satellite images. Furthermore, a kernel density map to illustrate RTS distribution and an analysis of RTS aspects employing a digital elevation model was conducted. To gain a better understanding of climate drivers of landslide occurrence a multifaceted approach of observational climate data, reanalysis on air temperature, precipitation and wind data as well as C-band backscatter data to derive soil moisture and the freeze/thaw soil state was performed.

The change detection of anthropogenic disturbance in 2013 showed a decrease of around 40 % compared to 2010: However, active landslides along the railway line can be seen despite of maintenance techniques. The occurrence of 81 RTS at lake margins are mostly located in the flat areas of the study area and are, in contrast to many other studies, less influenced by solar radiation since most of the landslide aspects are facing to the NW and N. The application of reanalysis in remote areas appears to be a beneficial tool, as it reflects the seasonal differences of continental and maritime influenced climate and shows high accuracy with backscatter soil moisture data in the study area. Thus, RTS triggering in 2012 could be attributed to a mild winter, early snow melt, high summer temperatures, and enhanced rainfall rates. Although RTS appears to be a natural phenomenon in the study area, anthropogenic impacts might contribute to the occurrence of RTS, as the biggest hotspot of RTS is observed in close proximity to the railway line.

Kurzfassung

Angesichts der Klimaerwärmung gehören eisreiche Permafrost-Landschaften zu den gefährdetsten Gegenden weltweit. Zusätzlich sind viele Gebiete in der Arktis von einer raschen industriellen Entwicklung betroffen, da natürliche Ressourcen durch verbesserte Verkehrsnetze und neue Technologien immer leichter zugänglich werden. Das Ziel dieser Studie ist es, anthropogene und natürlich hervorgerufene Störungen des Permafrostbodens zu untersuchen. Dabei soll insbesondere analysiert werden, ob es einen Zusammenhang zwischen Infrastruktur und dem Auftreten kryogener Erdrutsche gibt.

Die vorliegende Masterarbeit untersucht eine Region in Jamal, welche durch Bauarbeiten der Bovanenkovo Eisenbahnlinie, sowie durch regressive auftaubedingte Rutschungen in Folge eines sehr warmen, feuchten Jahres 2012 charakterisiert ist. Eine Veränderungsanalyse wurde mittels zwei hochauflösender optischer Satellitenbilder durchgeführt. Zudem wurde eine Kerndichteverteilung der Erdrutsche vorgenommen und ihre Hangausrichtung mittels eines digitalen Geländemodells analysiert. Für ein besseres Verständnis der klimatischen Ereignisse im Jahr 2012 wurden sowohl beobachtete Daten, Reanalysedaten bezüglich Lufttemperatur, Niederschlag und Winddaten als auch C-Band *Backscatter*- Daten zur Bodenfeuchte untersucht.

Die Veränderungsanalyse ergab im Jahr 2013 eine Abnahme der anthropogen verursachten Störungen um circa 40% im Vergleich zu 2010, jedoch konnten trotz Rekultivierungsmaßnahmen aktive Erdrutsche entlang der Bahnstrecke detektiert werden. Die an den Seeufern auftretenden Erdrutsche befinden sich größtenteils in topografisch flachen Gebieten. Die Erdrutsche sind zudem nicht vorrangig durch Sonneneinstrahlung beeinflusst, da die Mehrheit der Erdrutsche eine Hangausrichtung nach N und NW aufzeigen. Die Verwendung von Reanalysedaten zeigte sich als geeignete Methode, da die saisonalen Unterschiede von kontinentalem und maritimen Klima gut reflektiert wurden und eine hohe Übereinstimmung mit *Backscatter*-Daten aufzeigten. Die Initiierung der Erdrutsche kann demnach durch einen milden Winter mit früher Schneeschmelze, erhöhten Sommertemperaturen und höheren Niederschlagsraten erklärt werden. Auch wenn Erdrutsche ein natürliches Phänomen im Untersuchungsgebiet darstellen, scheint die Bahnlinie einen Einfluss darauf zu haben, da sich die größte Dichte der Erdrutsche in unmittelbarer Nähe zur Eisenbahnlinie befindet.

1 Introduction

The Arctic is affected by rapid climate change, which has significant impacts on permafrost regions and the world as a whole (Raynolds et al., 2014, Schuur et al., 2015). In the last 30 year's Arctic temperatures have risen 0.6°C per decade, twice as fast as the global average (AMAP; 2011, Schuur et al., 2015). This in turn leads to the degradation of ice-rich permafrost (Grosse et al., 2011) and modifies drainage, increases mass movements, and alters landscapes (Anisimov et al., 2007; Nelson et al., 2001; Romanovsky et al., 2010b). By the end of the 21st century, models predict a 30-70 percent decline in surface permafrost extent (Natali et al., 2014).

The effects of declining permafrost will affect the climate globally. The permafrost soils store approximately 1670 Pg of organic carbon, which is almost twice as much carbon as currently contained in the atmosphere (Schuur et al., 2009; Tarnocai et al., 2009). The thawing of permafrost can lead to the release of carbon to the atmosphere, which is considered to constitute a positive feedback mechanism to global warming (Heollesen et al. 2015; Lupascu et al., 2014; Schuur et al., 2015).

A seasonally thawed active layer overlies permafrost. Global warming and human-induced disturbances result in a deepening of the active layer and thaw settlement (Rowland et al., 2010). Recently, an increase in the frequency of cryogenic landslides could be observed in Canada and Northwest Siberia, demonstrating the relevance of this climate-sensitive process (Kokelj et al., 2017; Leibman et al., 2015; Segal et al., 2016).

Although permafrost regions are not densely populated, their economic importance has increased substantially in recent decades. This is related to the abundance of natural resources in the polar region and improved methods of hydrocarbon extraction, transportation networks to population centers and engineering maintenance systems (AMAP, 2011; Mazhitova et al., 2004; Nelson et al., 2002).

The Yamal Peninsula in Northwest Siberia is experiencing some of the most rapid land cover and land use changes in the Arctic due to a combination of climate change and gas development in one of the most extensive industrial complexes of the Arctic (Kumpula et al., 2006; Leibman et al., 2015; Walker et al., 2011). Specific geological conditions with massive tabular ground ice and extensive landslides intensify these impacts (Walker et al., 2011). The combination of high natural erosion potential and anthropogenic influence cause extremely intensive rates of erosion (Gubarkov et al., 2014). A considerable amount of recent work has focused on the effects of industrial development to ecological and social implications (Forbes, 1999; Kumpula et al., 2010; Walker et al., 2011). However, the interaction between infrastructure and morphological processes has been poorly studied.

This study aims to close this research gap by investigating the area surrounding Vaskiny Dachi that was affected by natural and anthropogenic large-scale disturbances within a three year's timeframe. The construction of the world's northernmost railway for the Bovanenkovo gas field was finished in 2010. In addition, the region experienced an extremely warm and wet summer in 2012, which resulted in the occurrence of cryogenic landslides. Currently, climate analysis is based on the closest climate station in Maare Sale, located on the coast around 120 km southwest of the study area (Leibman et al., 2015).

Hence, the objectives of this study are:

1) To map surface disturbances of Central Yamal between 2010 and 2013 using high-resolution satellite imagery
2) To quantify and analyze natural and anthropogenic impacts and the relation to each other in regards to permafrost degradation
3) To use reanalysis climate data on air temperature, precipitation and wind as well as backscatter data, to determine climatic factors influencing permafrost degradation in the study area.

2 Scientific Background

2.1 Permafrost

Permafrost is an essential part of the cryosphere and a key indicator of climate change (Romanovsky et al., 2010). It is defined as ground that remains frozen for at least two consecutive years and can be present in soil, sediment or rock (van Everdingen, 2005). Permafrost occupies about one quarter of the northern Hemisphere with the largest area in Russia (Nelson et al., 2002; Romanovsky et al., 2010a; Zhang et al., 2008). As depicted in figure 2-1 the permafrost distribution is divided into 3 main zones: continuous (covering 90 - 100 % of the underground), discontinuous / sporadic (10-90%) and isolated permafrost (0-10%) (Romanovsky et al., 2010).

Figure 2-1 Extent of permafrost in the Northern Hemisphere (http://www.grida.no/graphicslib/detail/permafrost-extent-in-the-northern hemisphere_1266, accessed 15 November 2016).

The regional permafrost extent is difficult to assess from direct ground surveys because of expensive and inconsistent in situ measurements (Duguay et al., 2005). Hence, indirect methods from remote sensing have been employed to monitor permafrost and obtain information about vegetation cover, ground thermal (air and surface temperatures) and hydrological parameters (snow depth and soil moisture) (Park et al., 2016). A coarse evaluation of permafrost can also be gained from sparse climate station and model reanalysis of interpolated station observations (Park et al., 2016).

2.2 Description of Permafrost Zones

The description of permafrost zones is depicted in figure 2-2.

Permafrost

Vertically, the permafrost zone extends from the permafrost table, which is located tens of centimetres to several meters below the ground surface depending on the conditions to the permafrost base several meter to 10^3 m deep (French, 2007).

Active Layer

Above the permafrost table ground temperatures exceed 0°C for some duration during summer, i.e. the surface layer thaws in summer and completely refreezes in winter (van Everdingen, 2005; Burn and Zhang, 2009). This seasonally thawed layer is called the active layer. The thickness of the active layer is defined as the maximum seasonal thaw depth (van Everdingen, 2005; Walvoord & Kurylyk, 2016). Although climate is the main parameter affecting the active layer thickness (ALT), it is governed by factors such as vegetation, soil conditions, topography and presence of water e.g. springfloods associated with the snowmelt (Shur & Jorgenson 2007; Trofaier et al., 2013). With deepening of the active layer, ground loses stability and is prone to degradation (Leibman et al., 2015).

Transition Zone

Below the active layer is the transition zone, an ice-rich layer that separates the active layer from the more stable permafrost below (Shur et al., 2005). This zone only thaws during summer and defines the boundary of the maximum long-term thaw depth of the permafrost (Walvoord &Kurylyk, 2016).

Sub Permafrost Zone

Perennially noncryotic conditions prevail beneath the permafrost base, due to the influence of the geothermal heat flux, which is illustrated in figure 2-2 (Walvoord & Kurylyk, 2016).

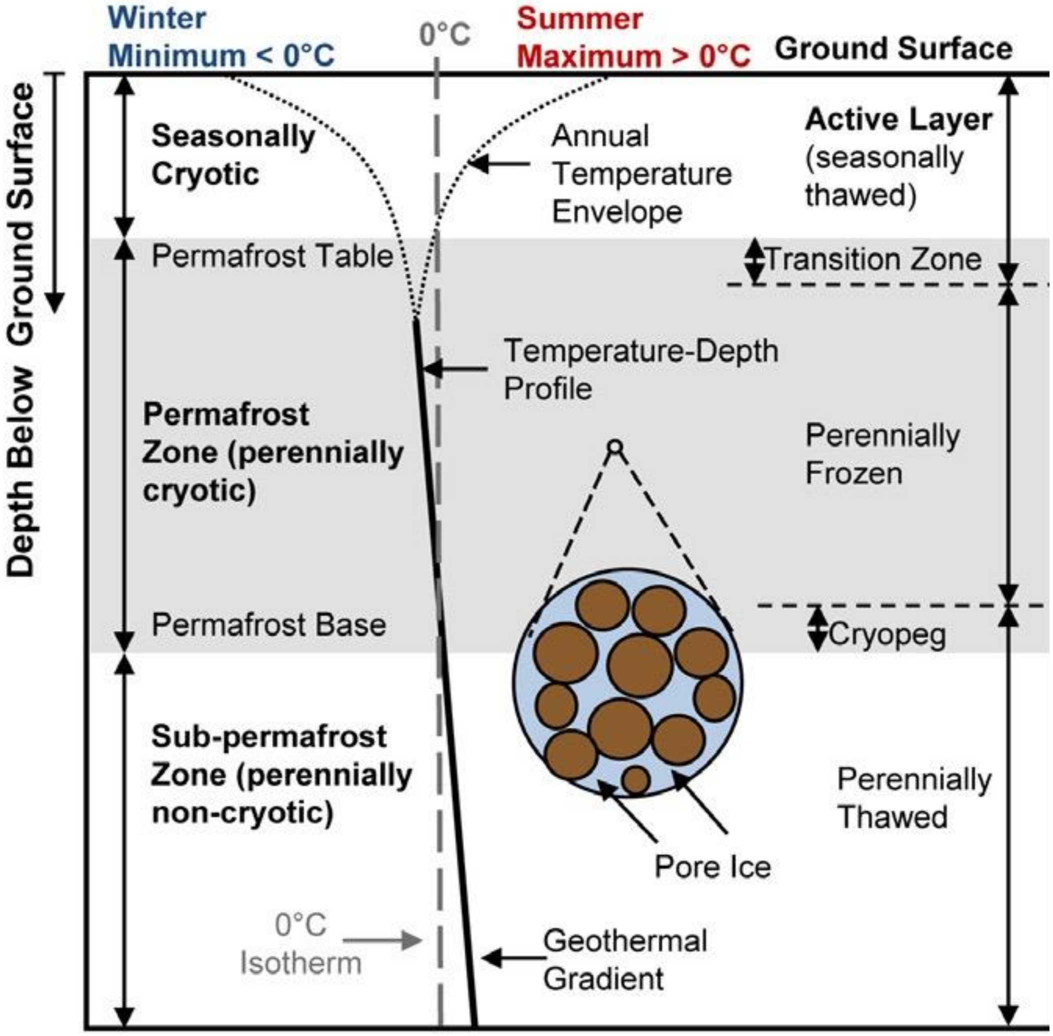

Figure 2-2 Permafrost zone descriptions and ground temperature profile after Walvoord &Kurylyk, 2016.

2.3 Ice-rich Permafrost and Tabular Ground Ice

Ice-rich permafrost contains ice volume exceeding that of soil pores (French, 2007). Ice-rich permafrost commonly consists of more than 40 % volume of ground ice in the form of segregated ice and massive ice-wedges (French & Shur, 2010). The ice occurs primarily in the upper 10 to 15 m of permafrost and is therefore sensitive to climate warming. Ice-rich permafrost extensively thawed during the early Holocene climate optimum forming numerous thermokarst lakes (Anthony et al., 2014; Séjourné et al., 2015).

A specific type of ice is tabular massive ground ice, which is defined by a gravimetric moisture content exceeding 250 % (dry weight) (Moorman, 1998;

Permafrost Subcomittee, 1988). It is widely distributed in the Arctic from the European North of Russia in westerly direction to Canada in the east (Rogov et al., 2003). It can form extensive ice deposits of about more than 20 m thickness in various depths (Walker et al., 2011). The origin of thick ground ice layers is still a subject of ongoing discussion (Walker et al., 2009; Fritz et al., 2011). The two main hypotheses consist of either buried Pleistocene glacial ice, or that it was formed in situ. Moorman et al., (1998) suggested that glacial melt water infiltration was responsible for the formation of intrasedimental ice. However, most references support the idea of tabular ground ice forming as a result of ground water migration under gradual freezing of exposed marine sediments either during regression of the sea, or with a rising landmass (isostatic or isostatic fall of sea level) (Leibman et al., 2003).

2.4 Permafrost Degradation

Permafrost landscapes have always been changing and affected by aggradation and degradation of frozen ground. However, in recent decades the intensification of global warming and increased economic usage in these areas resulted in increased disturbance frequencies and magnitudes (Grosse et al., 2016; Park et al., 2016)

The substantial permafrost retreat is associated with feedbacks ranging from local impact on topography, hydrology and ecology to complex influences on global scale biochemical cycling. The consequences often are irreversible on human time scales and may impact ecosystems, hydrology and carbon cycling for centuries to millennia (Grosse et al., 2016).

One important process of degradation is thermokarst, by which landscapes result from the thawing of ice-rich permafrost and/or melting of massive ice (Lantuit & Pollard, 2008; Kokelj & Jorgenson, 2013). The magnitude of thermokarst is directly linked to the thermal stability of permafrost including active layer and ground-ice content (Lantuit & Pollard, 2008). Thermokarst involves both, thaw subsidence and/or erosion (Lantuit & Pollard, 2005).

2.4.1 Mechanisms and Classification of Cryogenic Landslides

Cryogenic landslides are climate-related features and indicators of past and modern climate changes (Leibman et al., 2003). In permafrost zones landslides get triggered by high pore pressure due to water saturation provided by atmospheric precipitation together with melting of ground ice in the active layer and/or upper permafrost (Leibman et al., 2003). As seen in figure 2-3 two different mechanisms of landsliding in Arctic plains are classified*:* Active Layer Detachments and Retrogressive Thaw Slumps (Leibman et al., 2015).

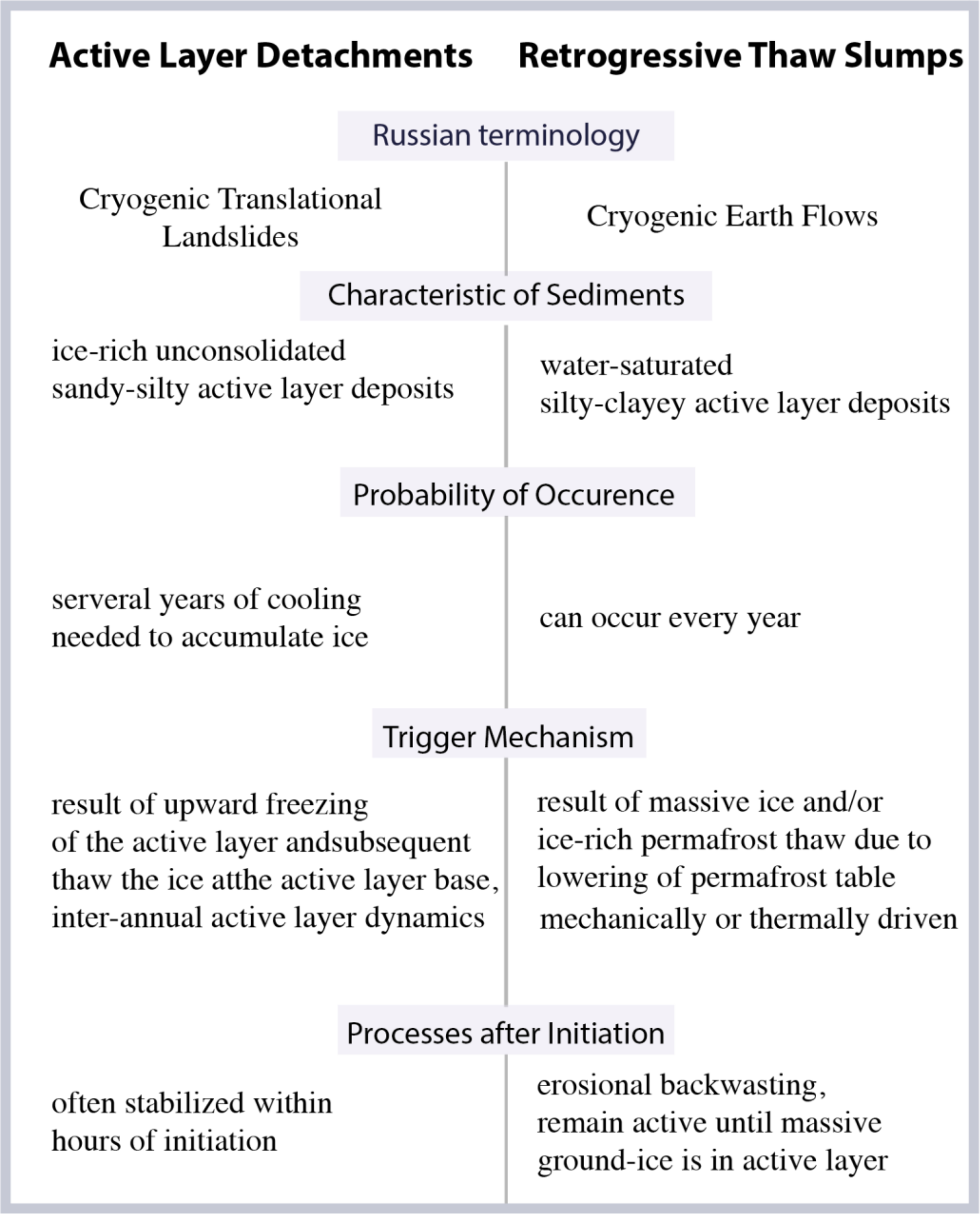

	Active Layer Detachments	Retrogressive Thaw Slumps
Russian terminology	Cryogenic Translational Landslides	Cryogenic Earth Flows
Characteristic of Sediments	ice-rich unconsolidated sandy-silty active layer deposits	water-saturated silty-clayey active layer deposits
Probability of Occurence	serveral years of cooling needed to accumulate ice	can occur every year
Trigger Mechanism	result of upward freezing of the active layer andsubsequent thaw the ice atthe active layer base, inter-annual active layer dynamics	result of massive ice and/or ice-rich permafrost thaw due to lowering of permafrost table mechanically or thermally driven
Processes after Initiation	often stabilized within hours of initiation	erosional backwasting, remain active until massive ground-ice is in active layer

Figure 2-3 Active Layer Detachments and Retrogressive Thaw Slumps in comparison according to Leibman et al., 2015.

Active Layer Detachments

Active Layer Detachments (ALD), also referred as Cryogenic Translational Landslides are slope failures restricted to the thawed active layer and typically occur in ice-rich unconsolidated sediments (Leibman et al., 2015; Rudy et al., 2016). The ice gets accumulated at the active layer base due to several years of cooling (French, 2007). Intensive heat flux and high precipitation rates trigger the rapidly thaw of the ice-saturated deposits at the active layer base. Thereby, excess water accumulates in the active layer because of low filtration ability of silty soils. The pore pressure rises dramatically leading to reduced effective shear strength and to the displacement of the surface (Rudy et al., 2016). ALD can expose massive ground ice that leads to increased ablation and the potential formation of RTS (French, 2007).

Retrogressive Thaw Slumps

Retrogressive Thaw Slumps (RTS), also known as Cryogenic Earth Flows in Russian literature, are a type of erosional backwasting thermokarst resulting from the exposure of ice-rich permafrost (Lacelle et al., 2010).

RTS are initiated through a variety of processes including (1) fluvial processes or shoreline wave-action (Lantuit et al., 2012), (2) thermally driven subsidence of lakeshores (Kokelj et al., 2009), (3) as a result of active layer detachments (Leibman et al., 2015), (4) anthropogenic impacts (Leibman et al., 2015) or/and (5) mass wasting triggered by increased active layer thaw or precipitation (Lacelle et al., 2010, 2015; Rudy et al., 2016).

RTS are characterized by a semi-circle-shaped depression also known as thermocirques that expose massive ice directly to surface energy fluxes (Figure 2-4). Thereby the stability depends on the size and orientation of the headwall, the ground ice content and surface energy fluxes (Leibman et al., 2015; Séjourné et al., 2015). RTS belong to the most erosive processes in periglacial environments with a headwall retreat of up to 8 m per year and remain active until massive ground ice is in the active layer (Lantuit et al., 2012). Thus, they can occur every year in contrast to ALD. The recent increases of thaw slumping in Canada (Segal et al., 2016) and North-West Siberia (Leibman et al., 2015) demonstrate the relevance of the climate-sensitive process (Kokelj et al., 2017).

Figure 2-4 Scarp and shear surface of cryogenic landslide (RTS) in Central Yamal (Picture by Y. Dvornikov, 2015).

2.4.2 Anthropogenic Disturbances

In areas of gas production and transportation facilities the erosional potential in ice-rich permafrost landscapes increases through direct and indirect impacts, such as

- changes in topography and hydrology,
- off-road vehicle use,
- petrochemical contamination,
- deterioration of the vegetation cover,
- increased snow storage due to accumulation near buildings and roads,
- exploitations of sand-pits, gas- and oil fields,
- increased sand/dust deposition.

Even small-scale, low-intensity anthropogenic impacts can lead to long-term changes in permafrost soils and tundra vegetation (Forbes et al., 2001; Kumpula et al., 2010). For example, off-road tracks can be visible for decades and alter surface and subsurface conditions in terms of surface energy balance and ground thermal properties (Yu et al., 2015). Waterlogging along the road network increases soil erosion as water has a smaller albedo than unperturbed vegetation and thus absorbs more heat (Yu et al., 2015; Gill et al., 2014). The recovery of disturbed tundra vegetation is typically slow and the reproductive rates of many arctic species are very low (Walker et al. 2011).

3 Study Area and Regional Setting

3.1 Yamal Peninsula

The Yamal Peninsula is located in northwest Siberia, Russia (Figure 3-1). It extends roughly 700 km from the Arctic Circle (66° 33.5'N) in the south to Ostrov Belyy (White Island, 73° 20'N) at the tip of the peninsula (Walker et al., 2011). It is bounded on the west and north by the Kara Sea, Baydaratskaya Bay on the west, and by the Gulf of Ob on the east (Walker et al., 2009).

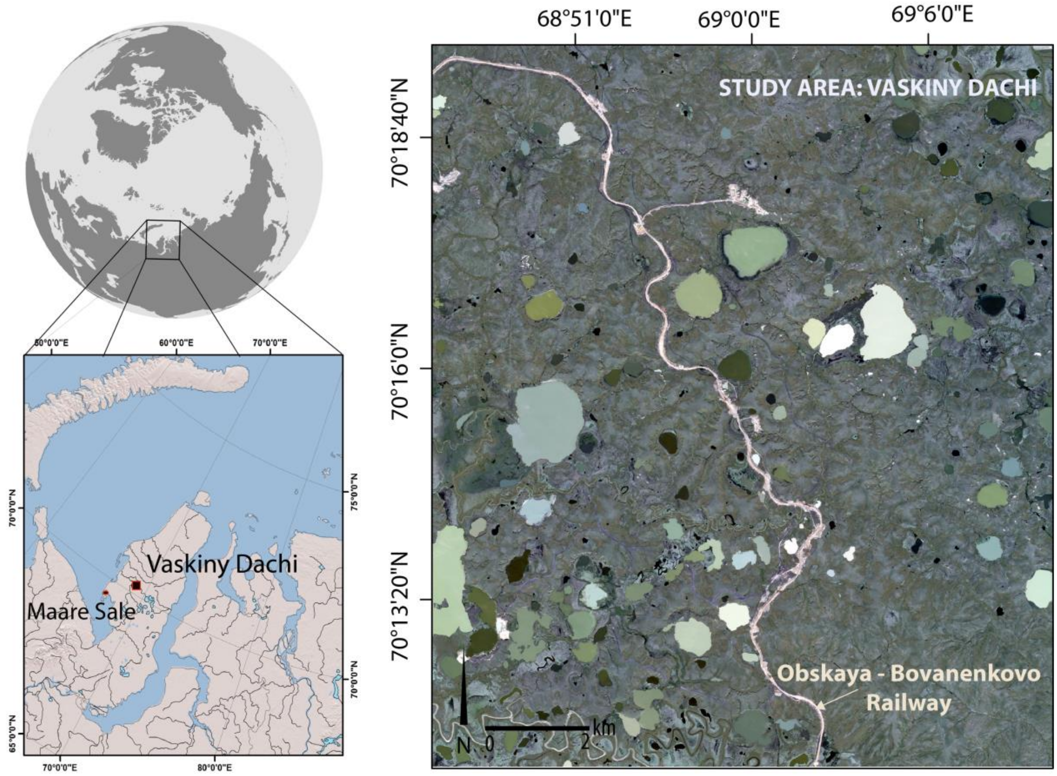

Figure 3-1 The study area Vaskiny Dachi is located in the zone of continuous permafrost in the center of Yamal Peninsula, northwest Siberia. The closest weather station is located in Maare Sale (world map downloaded from https://freevectormaps.com/world-maps, accessed 16 July 2016; ArcGIS Online Basemap modified after Y.Dvornikov (2016); study area: QuickBird: projection UTM 42N within WGS 84 datum.

The peninsula is characterized by a flat to gently rolling plain consisting of mainly marine, lacustrine and alluvial deposits. The oldest deposits are in the interior parts of the peninsula at elevations between 45 and 90 m a.s.l. and were deposited in the Mesozoic more than 130000 years ago. These sediments are mostly unlithified silts and clays (Forman et al., 2002). Lithified Paleozoic rocks occur south and west of the Yamal Peninsula in the Polar Ural Mountains and adjacent highlands (Forman et al., 2002). Most of the peninsula consists of Quaternary sediments deposited during and following the last glacial maximum (ca. 30000 – 12000 years ago), while the peninsula was unglaciated (Forman et al., 2002; Walker et al., 2009). Saline Quaternary deposits in the proportions typical of ocean environments can be found northward of 68°N, where permafrost did not degrade during the Holocene optimum (Streletskaya & Leibman, 2003).

Yamal Peninsula is located in the zone of continuous permafrost with permafrost thickness reaching its maximum of 500 m on the marine and coastal plains and reducing to 100-150 m at the younger terraces (Leibman et al., 2015). The distribution of tabular ice is at places very close to the surface (Dvornikov et al., 2015). Ice-rich permafrost is widespread and is susceptible to thermokarst erosion from both natural and anthropogenic surface disturbance, as well as climatic change (Forbes 1997).

Natural impacts in terms of landslide disturbances dominate the landscape in many areas (Leibman et al., 2015). They periodically modify slopes of the dissected middle to upper Pleistocene marine plains, exposing saline marine frozen soils. These disturbed areas show a specific type of tundra vegetation with high willows and richer biomass compared to the zonal vegetation (Leibman et al., 1995).

Yamal Peninsula encompasses four of the five Arctic bioclimatic subzones. Most of the peninsula is arctic tundra, north of latitudinal treeline (ca. lat. 66°30'N) (Forbes, 1997). The zonal vegetation ranges from low-shrub tundra in the south to sedge, dwarf shrub, moss tundra on Belyy Island (Walter et al., 2009).

The anthropogenic impact is rapidly expanding due to the vast reserves of gas deposits (Figure 3-2). To date the major infrastructure is concentrated in the area of the Bovanenkovo gas field with an extensive area of drilling sites around the railway corridor (Walker et al., 2011). The Bovanenkovo gas-field is the largest of the Yamal Peninsula with a total of proven reserves of around 4900×10^9 m^3. The so called "Yamal's Megaproject" developed by the company Gazprom is a long term plan to exploit the gas reserves and bring the gas to the markets. Thus, the economic usage of the area will rapidly increase (Walker et al., 2011). The

Bovanenkovo field was brought into production in 2012 and additional gas fields are being developed. There are also plans to build an airport and river port in the Bovanenkovo settlement (Forbes et al, 2009).

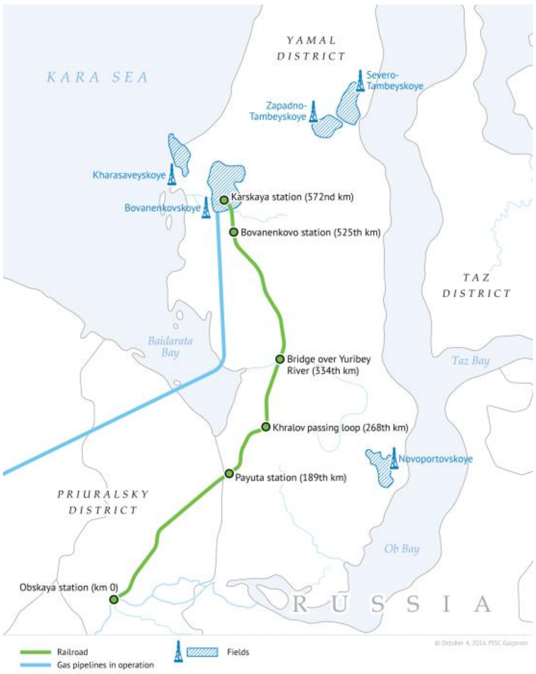

Figure 3-2 Yamal Peninsula is a hot spot for gas exploration. The 572 long Obskaya-Bovanenkovo railroad was finished in 2010 and is part of the Yamal megaproject. (http://www.gazprom.com/about/production/projects/mega-yamal/obskaya-bovanenkovo, accessed 22 February 2017)

One part of the Yamal megaproject was the construction of the northern-most railway. The Obskaya-Bovanenkovo railroad is 572 km long, from the Obskaya station to the Kaskaya station (Figure 3-2). The railroad was opened for traffic in 2011.

Off-road vehicle transport in the Yamal tundra has been prohibited since summer 1989. However, this restriction is routinely neglected, resulting in extensive surface disturbances (Forbes et al., 2001).

3.2 Vaskiny Dachi

3.2.1 General Characteristics

The study area is located at the watershed of Se-Yakha and Mordy-Ykha rivers in the vicinity of the Bovanenkovo gas fields (Leibman et al., 2015). The region is impacted by gas production development, reindeer herding by indigenous Nenets and climate change (Walker et al 2009b, 2010; Leibman et al., 2015). The most prominent landscape features are tundra lakes and river flood plains (Figure 3-3).

The topography is defined by highly dissected alluvial-lacustrine-marine plains and terraces formed by sandy and clayey deposits with elevations between 18 and 55 m a.s.l. (Leibman et al., 2015). Due to the marine origin in the late Pleistocene most of the sediments are saline and some are saline in the active layer (Leibman et al., 2015).

The highest marine plain Salekharskaya (V^{th}) with heights up to 58 m a.s.l. is built of saline clay with clastic inclusions of marine and glacio-marine origin. The surficial layer is washed out and shows non-saline silty sand enriched with clasts through wind erosion (Leibman et al., 2015; Trofaier & Rees, 2015).

The Kazantsevskaya coastal-marine plain is 40 to 45 m a.s.l. high and comprises alternating layers of saline clayey and sandy deposits with a considerable amount of organic matter. The surfaces are sometimes covered with windblown sands, but are mainly featured by tussocky, hummocky or frost-boiled tundras and peatlands in the lower areas (Leibman et al., 2015).

The third alluvial-marine or alluvial-lacustrine terrace is up to 26 m a.s.l. high, consists of fine interbedded sandy, silty, loamy, and organic layers of several millimeters to centimeters’ thickness. Flat hilltops are often characterized by polygonal sandy landscapes with windblown sand hollows on the tops of high-centered polygons. Lower terraces are of fluvial origin, including the flood plains of Modry-Yakha and Se-Yakha rivers and their smaller tributaries: Ngerm-Lymbadyakha, Panzananayakha, Khalmeryakha (Leibman et al., 2015; Trofaier & Rees, 2015).

Most of the study area consist of gentle slopes with angles less than 7°, 10 % of steep slopes with up to 50° and 30 % of the area are flat hill tops and depression bottoms. The slope comprises concave surfaces from ancient and modern landslides as well as convex surfaces from stable slopes (Leibman et al., 2015).

The study area is characterized by continuous permafrost. Open taliks are possible only under the larger lakes with 30–50 m depth. Smaller lakes, which are only several meters deep, have closed taliks (5–7 m thick). Cryopegs and layers with increased salinity have been found beneath the tabular ice at Central Yamal (Streletskaya & Leibman, 2003).

Figure 3-3 Landslides and lakes characterizing the study area, stabilized landslides are colonized by pioneer plants (pictures taken at the 25th of August 2015 by A. Bartsch)

3.2.2 Climate

The nearest climate station is in Marre Sale, which is located on the coast 120 km south-west of Vaskiny Dachi and thus characterized by a marine subarctic climate (Figure 3-1). The mean long-term annual air temperature is -8 °C (since the 1910's) and -7.7°C for the last 25 years. The annual precipitation rate varies greatly, oscillating between 200 and 400 mm, where about half falls as snow (8-8.5 months), and half as rain (3.5-4 months) (Leibman et al., 2015; Schuler et al., 2010). Over the last 10 years the annual mean temperature of January was -21.5 C° and in July 7.5°. The snow thickness on flat surfaces is up to 30 cm, while on leeward slopes of topographical depressions, such as gullies it can reach several meters (Khitun et al., 2015; Leibman et al. 2015).

3.2.3 Vegetation

The study region belongs to the arctic tundra zone in the bioclimatic subzone D. Plant growth is limited due to climate conditions and to the restriction of summer solar insolation. The vegetation is dominated by shrub willows (Salix glauca, S. lanata) and dwarf-birch (Betula nana) (Dvornikov et al., 2015).

Plant communities with dense shrub layers are mostly located in valley bottoms and gentle hill slopes. Willows grow up to 2 m in some places which affect snow distribution significantly (Dvornikov et al., 2015). On the watersheds dense dwarf shrubs are well developed. On gentle poorly drained slopes, low shrubs and dwarf shrubs are predominant and mosses are widespread. The hilltops are characterized by dwarf shrub-moss-lichen communities. On convex tops and windy hill slopes, shrub-moss-lichen communities are dispersed (Widhalm et al., 2016).

3.2.4 Active Layer Thickness

The spatial distribution of the Active Layer Thickness (ALT) depends on lithology and surface cover like the redistribution of snow, which results from strong winds and the highly dissected relief of Central Yamal (Dvornikov et al., 2015). The temporal fluctuations are controlled by ground temperature, summer air temperature and summer precipitation (Leibman et al., 2015).

Through the variety of surface deposits and vegetation cover, the ALT has a wide range of seasonal thaw depth. It reaches 40 cm under thick moss and up to 120 cm on sandy poorly vegetated surfaces (Leibman et al., 2015; Melnikov et al., 2004). Lowest ground temperature is characteristic for hilltops with sparse vegetation where snow is blown away. The warmest are areas with high willow shrubs, due to the retention of snow, found on slopes, in valleys and lake depressions (Widhalm et al., 2016). There are extremes observed on high centre polygons, where active layer depth exceeding 2 m (Leibman et al., 2015; Widhalm et al., 2016).

3.2.5 Cryogenic Landslides

Periodically hazardous processes such as thermal erosion and cryogenic landslides are taking place (Leibman et al., 2015). Cryogenic landslides in the study area increase from low (IInd-IIIrd) to high (IVth-Vth) geomorphic levels. The highest impacts occurred on concave ancient landslide-affected slopes and gentle slopes with tussocky shrub-sedge-moss cover on the Vth Marine plain (Leibman et al., 2015).

In August 1989, largescale cryogenic landsliding was observed in Yamal. Within an area of 10 km^2 in response to an abnormally wet year 400 new landslides occurred (Walker et al., 2011). The extremely warm summer of 2012 resulted in the formation of new thermal denudation features. The 2012 warm season was characterized by a 15 % deeper active layer than the average for the period of 1993-2011 (Khomutov et al., 2016; Leibman et al., 2015).

4 Material and Methods

This chapter provides an overview of the methods and data used in this study which are illustrated in figure 4-1. In the following, each dataset is briefly introduced and data processing methods are specifically explained.

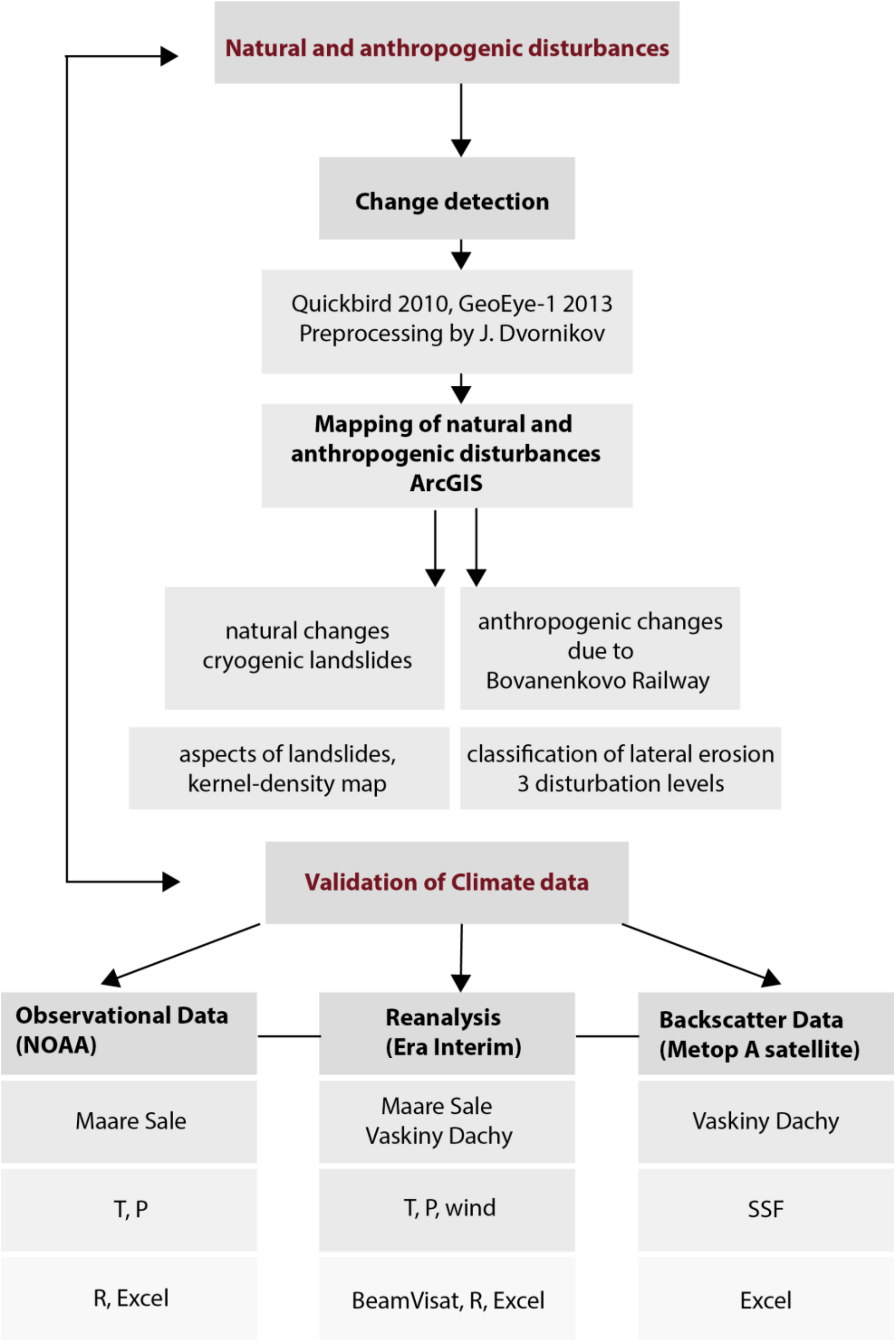

Figure 4-1 Overview of the methodological approach of the thesis.

4.1 GIS and Remote Sensing Data

Two high-resolution satellite images from the commercial satellites GeoEye-1 (acquisition date 05.07.2013) and QuickBird (acquisition date: 30.07.2010) were used in this study. The satellite images cover Central Yamal in the area of Vaskiny Dachi, where the railway for the Bovanenkovo gas field was constructed and many landslides occurred.

The images were pre-processed by J. Dvornikov in order to obtain a better stacking of the scenes and more appropriate spectral information. The pre-processing steps consisted of: (1) georeferencing using ground control points (GCP) collected in the field, (2) orthorectification using the TanDEM-X Digital Elevation Model (DEM) with 12 m spatial resolution, and (3) atmospheric correction using ACTOR module (Richter 1994) performed within the PCI Geomatica software. To increase image quality pan-sharped images were produced. GeoEye-1 served as a basis for georeferencing the QuickBird image, and the total Root mean square (RMS) errors are listed in table 4-1.

Table 4-1 Remote sensing data used in this study: pan-sharpening (PANSHARP2 model, Zhang 2004), orthorectification (OR) applied for all optical images using collected ground control points (GCPs) in the field with differential GPS Trimble 5700 and 12 m TanDEM-X digital elevation model (Dvornikov et al., 2016 a).

	Sensor/ Bands/ Scene ID	Aquired	Pansharped spatial resolution, m	Correction Procedures	RMS, m
Optical Data	GeoEye-1	2013-07-05	0.5	OR (GCPs, DEM)	0.37
	QuickBird	2010-07-30	0.6	OR (GCPs, DEM)	0.57
DEM	TanDEM-X	2013-06-19	12		

4.2 Mapping and Change Detection

The mapping of all human and natural impact features was performed with ArcGIS (10.3, ESRI) and based on the satellite imagery from 2010 (Quickbird) and 2013 (GeoEye-1). This was conducted within the Universal Transverse Mercator (UTM) projection zone 42 with the geodetic datum WGS 1984 using a scale of 1:3 000 Additionally, photographs from the field work in 2015 taken by A. Bartsch, and expert advices given by Y. Dvornikov, B. Heim and A. Bartsch, served as a basis for the analysis and interpretation of the mapped features.

4.2.1 Anthropogenic Impacts – Construction of Railway

The main anthropogenic impact in the area results from the construction of the railway. The railway was digitized as a polyline in ArcGIS. A buffer around the polyline of 100 m was created based on the study of Yu et al., (2015), who observed the most directs impacts from the industrial disturbance within this distance. For indirect impacts like hydrologic changes, which can occur several kilometres from the direct impact (Gill et al., 2014; Trofaier et al., 2013), the highest kernel density distribution of landslides near the railway was used as a key site.

The heterogeneous pattern of the railway disturbance was mapped as polygons in the satellite images taken from 2010 and 2013. The disturbed areas adjacent to the railway were visible through brighter colors. However, difficulties arose where no distinct spectral difference between the disturbed and the undisturbed zone could be distinguished. Thus, the Normalized Difference Vegetation Index (NDVI) was used as a proxy for detecting surfaces with reduced vegetation cover (Rudy et al., 2013). The principle behind NDVI takes advantages of the different absorption and reflectance characteristic of vegetation in the red and near infrared (NIR) region of the electromagnetic spectrum. The chlorophyll in vegetation highly absorb visible red light, while the internal structure of the vegetation causes high reflectance in the near infrared region (Tucker, 1979). The NDVI is calculated by the following band ratio:

$$NDVI = \frac{NIR - RED}{NIR + RED} \tag{4-1}$$

NDVI is a dimensionless radiometric measure that ranges from -1 for non-vegetated surfaces to +1 for healthy productive vegetation (Tucker, 1979).

In addition, the housing of workers, quarries and parking areas were mapped to calculate the total anthropogenic disturbance in 2010 and 2013. Off-road tracks are not included in the analysis because they were difficult to see in the QuickBird satellite image.

Classification of Railway Disturbance

The degree of change was classified into three major disturbance levels—low (M1), medium (M2), and high (M3)—based on the width of disturbance and magnitude of change over the course of three years (see table 4-2).

Table 4-2 Classification of railway disturbance (Appendix A1, Figure A-1)

M1	**Low disturbance level** Disturbed area shows a decrease from 2010 to 2013 due to revegetation, lateral disturbance is less than in classes M2 and M3, disturbance pattern is homogenous
M2	**Medium disturbance level** disturbed area shows a decrease from 2010 to 2013 due to revegetation, lateral disturbance is higher than in M1 with more irregularities
M3	**High disturbance level** disturbed area shows a slightly decrease from 2010 to 2013, however, new landslides occurred adjacent to the railway and an increase in lateral erosion can be observed in 2013, inhomogeneous disturbance pattern

The classification of table 4-2 was evaluated by using an area/length (m^2/m) ratio according to the disturbed section M1, M2 and M3 for 2010 and 2013, respectively. This ratio was correlated with the other disturbed sections to see the percentage of every section and the percentage of area change over the 3 years.

4.2.2 Natural Impacts - Cryogenic Landslides

The landslides in the area were mapped in the 2013 GeoEye-1 image. Landslides are manually digitized as polygon features by J. Dvornikov (2014). In order to see the predominant landslide direction, the aspect, which bounds to the lake margin was calculated using the TanDEM-X with a resolution of 12 m.

The landslides pattern across the study area was visualized using the kernel density tool in the Spatial Analyst. Therefore, the polygons were converted into points with the Polygon to Point function. The kernel density places a symmetrical surface over each point, evaluating the distance from the point to the cell. Points closer to the cell are given a higher weight in the density calculation than points further away from the cell. The result is a visualisation of the spatial frequency of the landslides over the study area (Okabe et al., 2009).

4.3 Validation of Climate

In the study area, no meteorological station exists. The closest station is located in Maare Sale, which is situated roughly 130 km to the west from the study area. To verify whether the climate data from Maare Sale is representative for the study area in Vaskiny Dachi, reanalysis data from Era Interim were compared for the years 2011 to 2015. A climate characteristic of Vaskiny Dachi was then performed for the years 2007 – 2015.

4.3.1 Reanalysis Data

Reanalysis is a helpful tool to assess climate change and variability, especially in the Arctic where meteorological records are spatially sparse (Bromwich et al., 2007). Reanalysed meteorological data provides an approach to produce spatially and temporally complete atmospheric parameters. This allows for the flexibility of collecting data from anywhere in the world. It includes a complex atmospheric model and uses remote sensing as well as in situ observations derived from ships, drifting buoys and land stations to verify the model outputs (Berrisford et al., 2011; Dee et al., 2011).

In this study Era Interim data is used, which has been validated to produce reliable air temperatures for the Arctic (Dee et al., 2011; Screen & Simmons, 2011). It is the latest atmospheric reanalysis product by the European Centre for Medium-Range Weather Forecast (ECMWF). Data is freely available and can be downloaded from January 1979 until present and is being updated regularly. Era Interim uses a spectral Global Gaussian grid horizontal resolution (T255) which corresponds to roughly uniform 79 km spacing (Dee et al., 2011). The surface archive has a mixture of analysis fields and accumulated forecast fields and is available globally at 6 hour's intervals.

Pre-processing of Reanalysis Data

Global data sets were downloaded at NetCDF files and loaded into Beam Visat, an open-source program for viewing, analyzing and processing of raster data. The information of the geographical coordinates was clipped and extracted as a text file. The location of the coordinates of Maare Saale emerged as a land-water pixel. Owing to different climate aspects at the sea, the pixel was changed to the adjacent pixel in the east direction to obtain a land based pixel.

Further processing of data was applied by RStudio. Data is brought into the correct order to assign every data point to a specific date and to calculate daily mean values. For the illustration of the monthly temperature and precipitation data, the Walter-Lieth diagram was chosen, and wind data was displayed in a rose diagram. The scripts can be seen in in the Appendix A1.

Air Temperature and the Calculation of the Thawing/Freezing Index

Temperature is reanalysed for 2 m above ground. Data was downloaded from Era Interim Daily at 0.00 and 12.00 UTC and step 0 was chosen to obtain the temperature at exactly this time. Temperatures in K were converted into °C:

$$°C = K - 273.15 \tag{4-2}$$

In order to evaluate the active layer dynamics, the thawing index (TI) and freezing index (FI) was calculated. The index is defined as the seasonal integrated

summer temperatures result in an increase of ALT (Streletskiy, 2015). The estimation of the FI and TI was based on the daily mean value and was calculated as the sum of the average daily temperatures for all days with below (FI) and above (TI) 0°C (Frauenfeld et al., 2007).

The FI is calculated as:

$$FI = \int_{t_0}^{t_1} |T| dt, T < \ 0°C \tag{4-3}$$

, where the FI corresponds to Era Interim air temperature integrated from the beginning t_0 to the end of the freezing t_1 season as shown in figure 4-2.

The TI is the integral of the air temperature from the beginning t_1 to the end of the thaw period t_2:

$$FI = \int_{t_1}^{t_2} |T| dt, T > \ 0°C \tag{4-4}$$

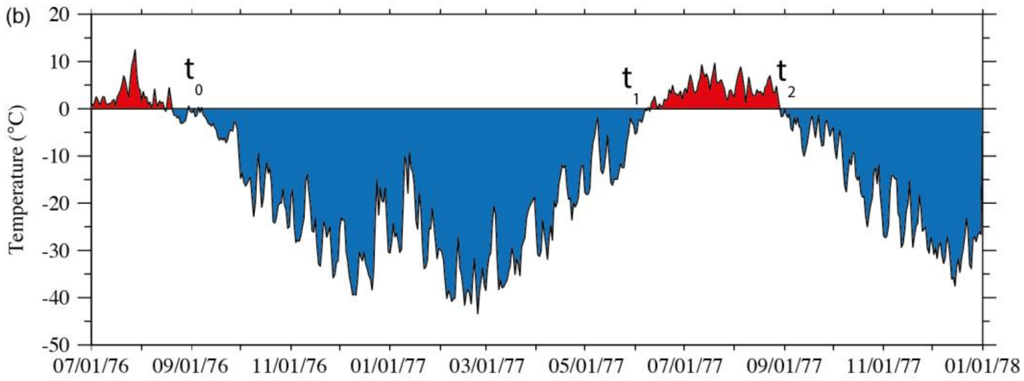

Figure 4-2 Example of a high latitude station, where the freezing/thawing index corresponds to the time series in blue and red, respectively (modified after Frauenfeld et al., 2007).

Wind

Era Interim data consists of the u (eastwards) and v (northward) orthogonal vector components of the wind field at 10 m above ground level.

By using trigonometric functions wind direction (θ) and wind speed (ws) can be calculated.

$$U_{geo} = ws * \cos(\theta) \tag{4-5}$$

$$V_{geo} = ws * \sin(\theta) \tag{4-6}$$

The average wind speed is calculated using the Pythagorean theorem:

$$ws = \sqrt{{U_{geo}}^2 + {V_{geo}}^2} \tag{4-7}$$

The geographic wind direction Dir_{geo} is the direction with respect to true north, (0=north, 90=east, 180=south, 270 = west) where the wind is coming from.

To obtain the wind direction the vectors have to be inverted to get the mathematical direction. This is the direction the wind is blowing to, counter-clockwise from the positive x-axis. The atan2(U,V) function is used to gather information of the appropriate quadrant of the calculated angel as depicted in figure 4-3. For this degrees are converted to radiant. If the value is less than zero 360 is added.

$$Dir_{geo} = atan2\left(-U_{geo}, -V_{geo}\right) * \frac{180}{\pi} \tag{4-8}$$

Wind data is then split into summer and winter months, averaged over time to produce a seasonal wind pattern. The calculation is based on information of the soil moisture data and SSF from backscatter data (see chapter 4.4.3).

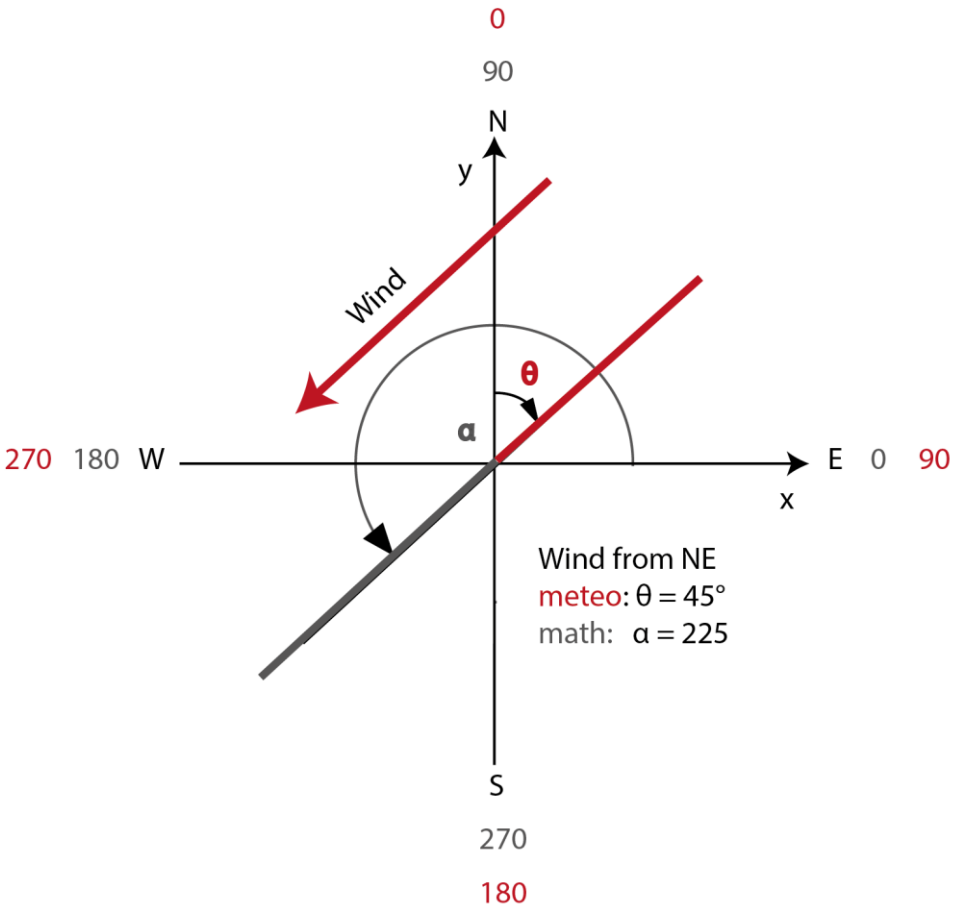

Figure 4-3 Converting from meteorological direction to mathematical direction

A frequency histogram of wind speed was compiled to get an appropriate classification for the wind roses. According to this, the wind speed is classified into 4 groups based on the Beaufort scale, an empirical measure that refers to observed conditions at land (Wheeler & Wilkinson, 2004). The classification can be seen in table 4.3. To see the seasonal difference of wind direction and wind speed, winter was defined as the period of air temperatures below 0°C, which was on average from October to end of May and the summer was defined from June to September.

Table 4-3 Classification of the wind speed, using the Beaufort scale (Wheeler & Wilkinson, 2004).

Beaufort number	Description	Wind speed	Land conditions
0-4	Calm to Moderate breeze	< 0.3 – 7.9 m/s	Calm to leaves and small twigs constantly moving
5	Moderate breeze	8 - 10.7 m/s	Branches of a moderate size move
6	Strong breeze	10.8 - 13.9m/s	Large branches in motion
7	High wind, moderate gale, near gale	13.9 – 17.1 m/s	Whole trees in motion

Precipitation

Precipitation is an accumulated forecast field and was treated differently compared to the analysis fields of temperature and wind. Data were downloaded from Era Interim Synoptic Monthly Means at 0.00 and 12 UTC and step 12 was chosen to capture the whole day. (Step 12 corresponds to 12 hours accumulated values from 12 and 00UTC). The unit of precipitation was in m. To get mm/day the two values are added and multiplied by 1000 to get mm/day.

4.3.2 Observational Data

Since the accuracy of reanalysis in Arctic regions is not well known (Lüpkes et al., 2010), reanalysis data were compared with observational data of the Marre Sale station. Data were freely available on National Ocean and Atmospheric Administration (NOAA, https://www.ncdc.noaa.gov/cdo-web/). The web contains datasets from global automated weather observing systems (AWOS).

Data were processed for temperature and precipitation from 2011 to 2015. The data were aggregated for daily averages to compare with ERA-Interim data described in chapter 4.3.1. Temperature was given in °F and had to be converted into °C:

$$°C = \frac{(°F - 32)}{1,8} \tag{4-9}$$

Precipitation were given in inch and was converted to mm:

$$mm = inch * 25.4 \tag{4-10}$$

4.3.3 Pearson Correlation

The climate trends of the observed and reanalysed climate data as well as the climate trend of Maare Sale and Vaskiny Dachi was evaluated using the Pearson correlation coefficient (r). The Pearson correlation is a measure of the linear dependence between two or more variables and is calculated by the following equation (Hartung, 1999):

$$r = \frac{\sum_{i=1}^{n}(x_i - \bar{x})(y_i - \bar{y})}{\sqrt{\sum_{i=1}^{n}(x_i - \bar{x})^2 \sum_{i=1}^{n}(y_i - \bar{y})^2}} \tag{4-11}$$

, where s_{xy} is the empirical variance, s_x and s_y the empirical standard variations, $\bar{x}$ and $\bar{y}$ the mean values of the to be correlated variables x and y as well as the number of value pairs. It has values from -1 (total negative linear correlation) to 0 (no linear correlation) to 1 (total positive linear correlation).

4.3.4 Deriving Soil Moisture from Backscatter

Information on soil moisture is valuable, since variations of freeze/thaw conditions have substantial impact on the active layer development and thermal denudation processes in permafrost regions (Shiklomanov et al., 2010; Naeimi et al., 2012).

In this study c-band backscatter data from ASCAT onboard Metop-A satellite is used to verify the reanalysis data and to get a better understanding of the soil conditions of the study area.

Microwave backscatter differs significantly between frozen and unfrozen due to changing dielectric properties that occur as water transitions between solid and liquid phases (Bartsch et al., 2011; Kimball et al., 2001; Naeimi et al., 2012). The high dielectric constant water is the result of water molecules alignment of its electric dipole in response to an applied electromagnetic field (de Ju et al., 2008). The penetration of microwaves generally decreases as moisture level increases (Kimball et al., 2001). When the soil surface begins to freeze the dielectric constant strongly decreases as molecules become unable to align. As a result, the backscatter drops. With increasing temperatures in spring, the snow melts and water covers the surface, which leads to a sudden drop in backscatter. In summer backscatter is increasing due to vegetation growth and high soil moisture (Park et al., 2011; Naeimi et al., 2012, Figure 4-3).

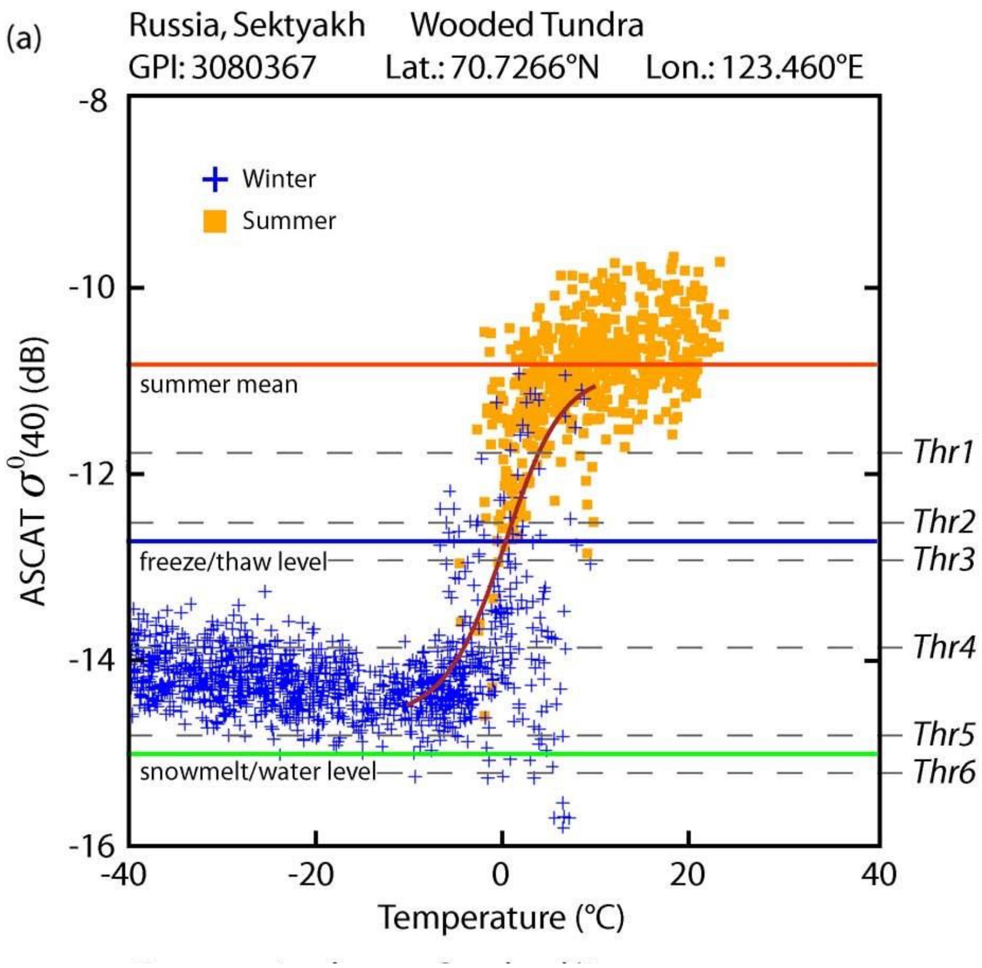

Figure 4-4 Example of backscatter versus temperature from Russia, Sektyakh. The dashed lines show the thresholds used in the SSF decision trees (Naemi et al., 2012)

As shown in several studies active c-band scatterometer data show high potential to provide soil moisture information. Naeimi et al. (2012) developed a so-called Surface State Flag (SSF) data using an empirical threshold analysis algorithm together with soil temperature data from the ECMWF reanalysis (Figure 4-4). The SSF identifies surface conditions between 1) Unfrozen, 2) Frozen, 3) Snowmelt /water on surface and 4) unknown. Backscatter data is freely available through the data archive PANGAEA. Daily mean values of SSF and soil moisture were calculated for different amounts of measurements per day.

5 Results

In the first part, the results of the anthropogenic and natural change detection will be examined on the basis of two high resolution images in 2010 and 2013. In the second part, the applicability of reanalysis data on the study site will be accessed to determine climatic factors influencing permafrost degradation. This will be performed by a comparison of the nearest weather station in Maare Sale and backscatter data from Metop-A satellite.

5.1 Anthropogenic Change Detection

The area of interest covers 266.3 km^2 in Central Yamal and is situated in the south-west of the Bovanenkovo gas field. The length of the analysed railway line in the study area is 22.12 km, which is 3.8 % from the total length of the Bovanenkovo railway line (572 km).

Anthropogenic Impacts in 2010

The total direct anthropogenic impact was 3.49 km^2 in 2010 (1.3 % of the study area) including the Bovanenkovo railway line, two sand quarries and the access roads to them, two parking lots and housings and four bridges for the railway line. The lateral disturbance by the railway itself is 2.54 km^2. The construction work is ongoing since housing and parking areas with a total disturbed area of 0.26 km^2 and sand quarries with a disturbed area of 0.69 km^2 (including access roads) are still in usage. The highest disturbance can be seen where bridges crosses streams and where the railway line is close to lakes, seen in a different water color caused by high sediment suspension (Figure 5-1).

Anthropogenic Impacts in 2013

The total impact decreased from 3.49 km^2 to 2.36 km^2 (see table 5-1). The disturbance area of the railway decreased from 2.54 km^2 in 2010 to 1.59 km^2 in 2013. Most parts of the areas close to the embankment look stabilized through natural vegetation recovery and maintenance techniques. The facilities for the construction are not in use anymore and look in most parts stabilized, overgrown by new vegetation cover. Nevertheless, the spatial resolution does not allow detecting small scale impacts in terms of industrial trash. The areas around the bridges seem to be stabilized through maintenance techniques. However, active thaw settlement can be observed as shown in figure 5-1.

Table 5-1 Overview of calculated disturbances of anthropogenic impact (Appendix A1, Figure A-2)

	2010	**2013**
• Total direct anthropogenic impact (excluding off-road tracks)	~3.49 km^2	~2.37 km^2
• Railway disturbance including 4 Bridges	~2.54 km^2	~1.58 km^2
• two quarries and two access road to quarries	~0.69 km^2	~0.67 km^2
• two parking lots/housings	~0.26 km^2	~0.12 km^2

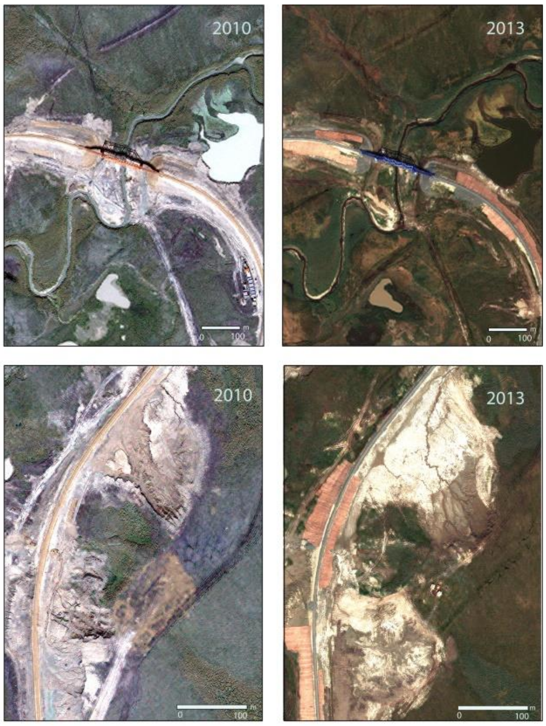

Figure 5-1 Comparison of the hot spot areas in the study area in 2010 and 2013. The construction of the bridge shows high disturbance level in 2010 and seems to be in most parts stabilized in 2013. An increase of thaw settlement can be seen in the lower pictures in 2013.

5.1.1 Classification of Disturbance Level

The description of the disturbance classification can be seen in chapter 4.2.1.

Table 5-2 compares the disturbed area of each class. To make each class comparable to each other the disturbance area per meter for every year was calculated and related to entire length of the railway. The lateral disturbance average in 2010 is around 114.9 m^2/m and varies from section M1 of around 80.4 m^2/m (22% of disturbance average) to railway section M2 of around 112.0 m^2/m (31 % of disturbance average) to railway section M3 of around 168.1 m^2/m (47 % of disturbance average).

In 2013, all sections show a decrease in disturbance area. The average disturbance per meter is 71.5 m^2/m and varies with the same succession from M1 of around 46.81 m^2/m (20% of disturbance average), to M2 with 66.88 m^2/m (28% of disturbance average) and M3 with 125.29 m^2/m (52 % of disturbance average). Comparing the classified sections of the railway line with the DEM it is noticeable that the highest disturbance of the railway line occurs in the flat areas as depicted in figure 5-2.

Table 5-2 Overview of the railway classification showing the calculated area per meter with respect to the length of the line (see table 4-2 for classification criteria).

	Length of railway	**Length of railway M1**	**Length of Railway M2**	**Length of Railway M3**
(in m)	22.12 km	5.518 km	14.32 km	2.92 km
%		24.94 %	61.9 %	13.2 %
	Disturbance area	**Disturbance area M1**	**Disturbance area M2**	**Disturbance area M3**
2010	2.54 km^2	0.44 km^2	1.60 km^2	0.49 km^2
2013	1.58 km^2	0.25 km^2	0.95 km^2	0.36 km^2
	m^2/m			
2010	114.88	80.44	112.04	168.11
%		22.3 %	31.07 %	46.62 %
2013	71.57	46.81	66.88	125.29
%		19.58 %	27.98 %	52.42 %

5.2 Natural Change Detection

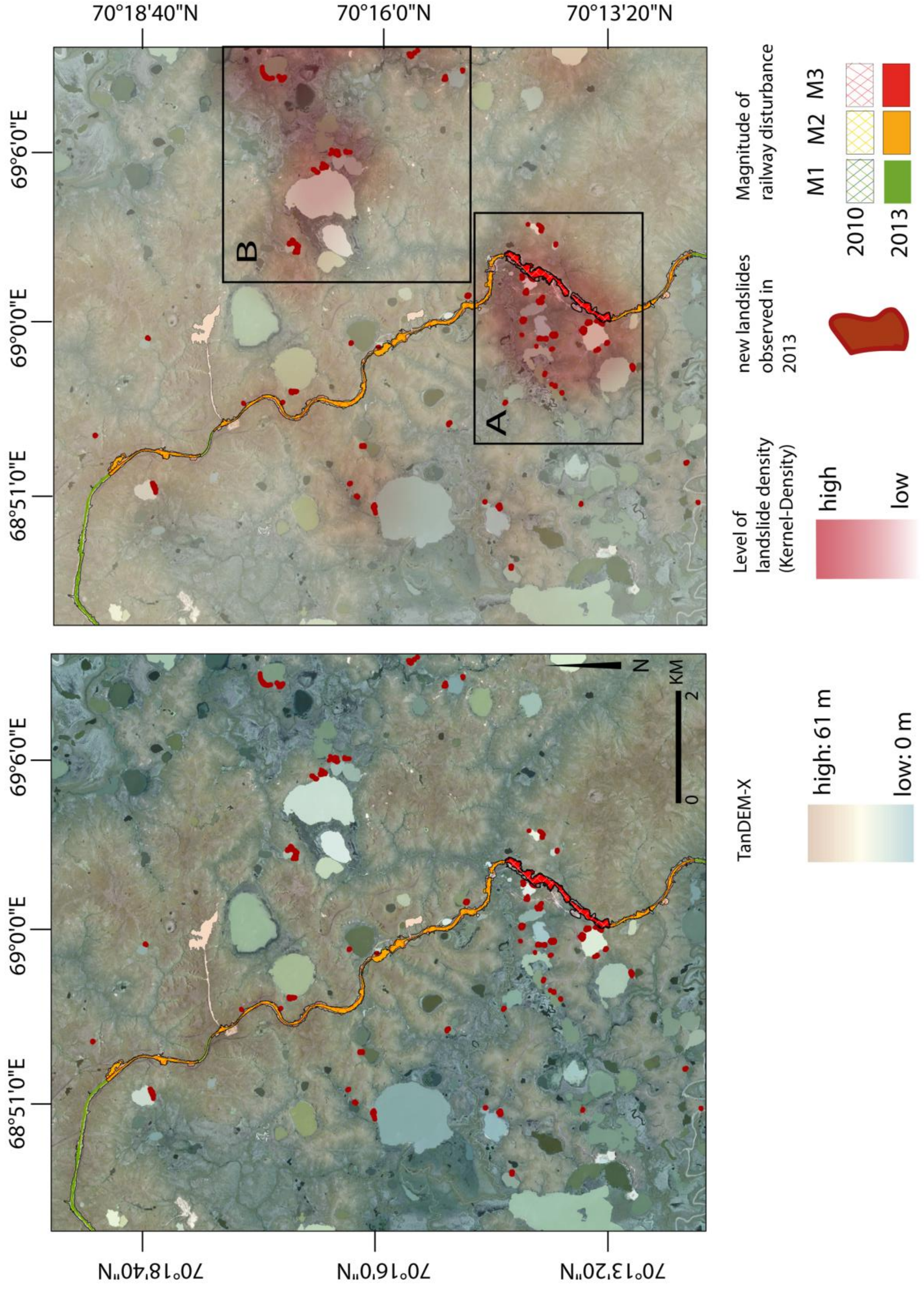

Figure 5-2 The study area of Vaskiny Dachi with the disturbance classification of the railway line and the two key sites A and B. The landslide distribution is illustrated with the kernel density map, background image: QuickBird, natural color composite and TanDEM-X for illustrating terrain factors, projection UTM Zone 52 N within WGS 84 datum.

In the study area a number of 81 active RTS ranging from 114 m^2 to 7660 m^2 with an average size of 1953 m^2 were detected in the Geoeye-1 image. A total disturbed area of 0.159 km^2 was affected. Eight of the landslides are adjacent to the railway in means of a distance of < 100 m. The RTS are distributed in the whole study area at the lake margins and are mostly located in flat areas and in the vicinity of flood plains.

5.2.1 Comparison of the Two Hotspots

The kernel density distribution of landslides seen in figure 5-2 shows two major hotspots. The highest density of landslides is adjacent to the railway line in the section of disturbance level M3. The hotspot can be seen in figure 5-3. In the area of interest 33 landslides can be observed within an area of around 20.3 km^2. The total affected area was 0.051 km^2. In the key site 10 lakes are influenced by a range of one to five RTS per lake. Most of the RTS are distributed in the vicinity of the floodplain area and are bounded to higher terrain.

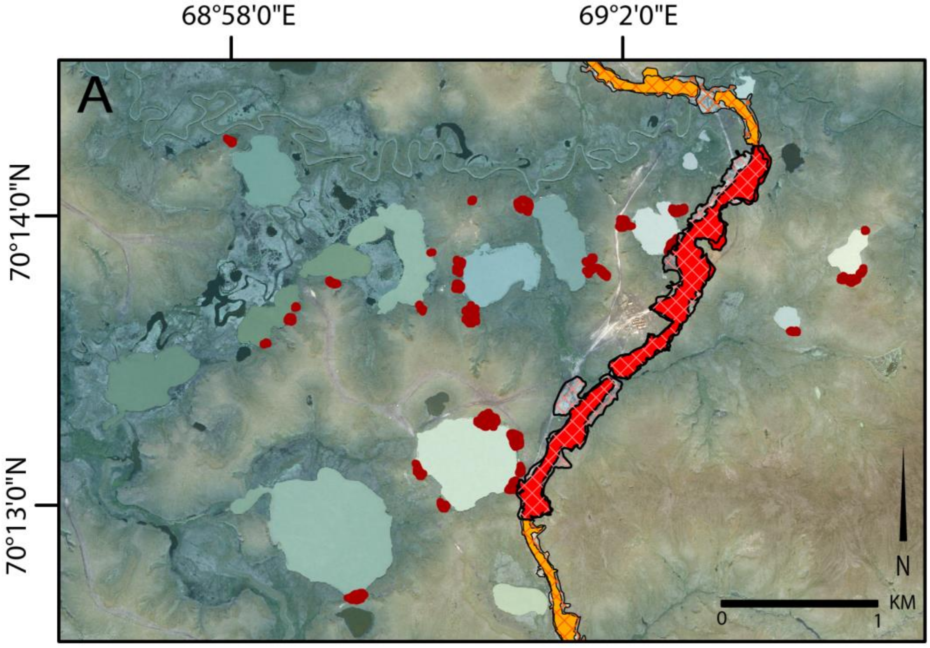

Figure 5-3 Key site A of landslide distribution (see figure 5-2). The landslides are located in the vicinity of 1) a floodplain, 2) the railway line in the section of disturbance level of M3 and 3) off-road-tracks, sometimes very close to the lake margins. Background image: Quickbird and TanDEM-X projection UTM Zone 52 N within WGS 84 datum.

The key site B is located in a distance of around 2 to 4 km NW of the railway line (Fig. 5-2). The key site seen in figure 5-4 has a size of 40.02 km^2. The 18 detected RTS affecting eight lakes and are more dispersed compared to key area A. The number of landslides of every lake is not correlated with the lake size as seen in figure 5-4. The total disturbed area was calculated to 0.054 km^2, which show that the size of the respective landslides is than in key area A. Most of the landslides occurred on lake margins and bound to slopes.

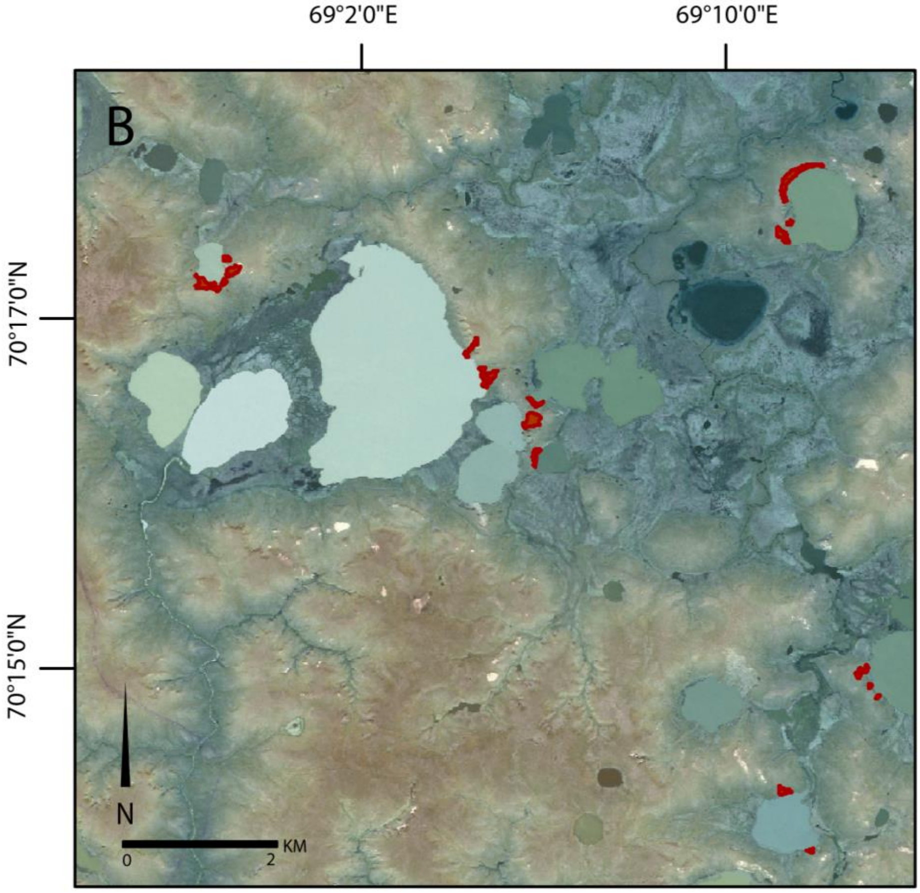

Figure 5-4 Keysite B of landslide distribution (see figure 5-2), which is unaffected by anthropogenic impact. The landslides are mostly located in flat areas and bounded to slopes. Background image: Quickbird and TanDEM-X, projection UTM Zone 52 N within WGS 84 datum.

Aspect Analysis of Landslides

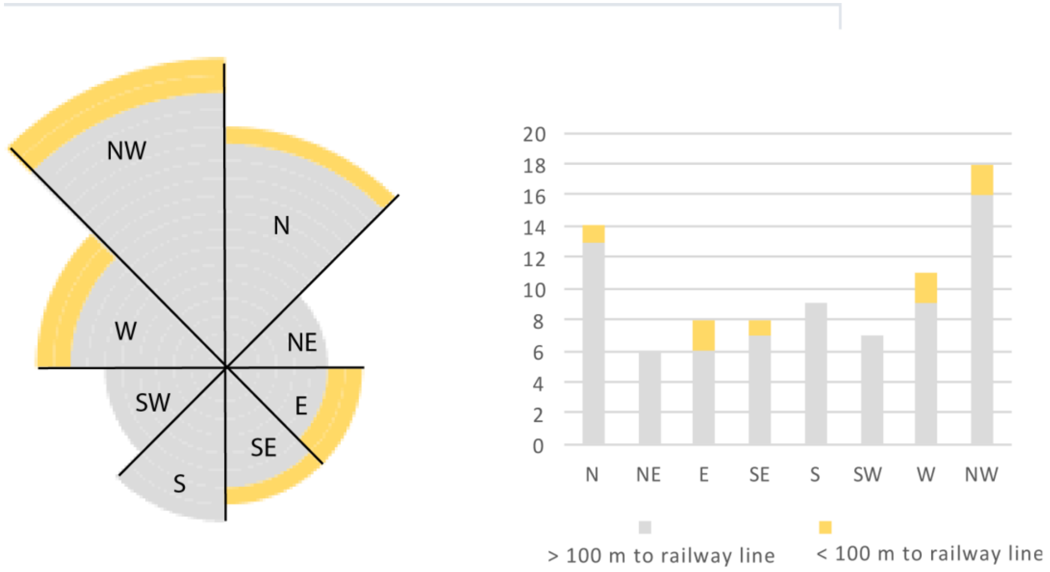

Figure 5-5 Aspect-rose diagram and related frequency histogram of the 81 landslides in the study. A differentiation between landslides within a distance of 100 m to the railway line and outside of the railway line was accomplished. The majority of landslides are facing to the NE and N.

In figure 5-5 the aspect-rose diagram of landslides and the related frequency diagram are illustrated. Landslides within the 100 m threshold are oriented to the course of the railway line. However, the influence of off-road tracks and indirect impacts of the railway line was not considered. Of the 81 landslides which were mapped, the majority (n = 18) facing to the NW, whereby two of them are in a distance of < 100 m to the railway line. The second highest occurrence of landslides facing to N (n = 14), whereby one is located in the 100 m threshold. Landslides facing to the SW, S, SE and NE are less affected by landslides initiation.

5.3 Comparison of Reanalysis and Observed Climate Data

The observed data downloaded from NOAA for the coastal station Maare Sale were compared with grid cell reanalysis data from Era Interim. The grid cell does not represent the same location as the observed station due to the mixed-pixel problem described in chapter 4. The Era Interim grid cell is located in the eastward direction, approximately 50 km further inland.

Temperature

There is a good agreement between observed and measured temperature in Maare Sale. The Pearson correlation coefficient is very high with r = 0.97. The average difference is 0.4°C degrees and the highest deviations can be seen in winter. Monthly accumulated data reflect the high accordance as shown in figure 5-6. Era Interim shows no trend in higher or lower temperatures over the year; 46 % of measurements show slightly higher Era Interim temperatures.

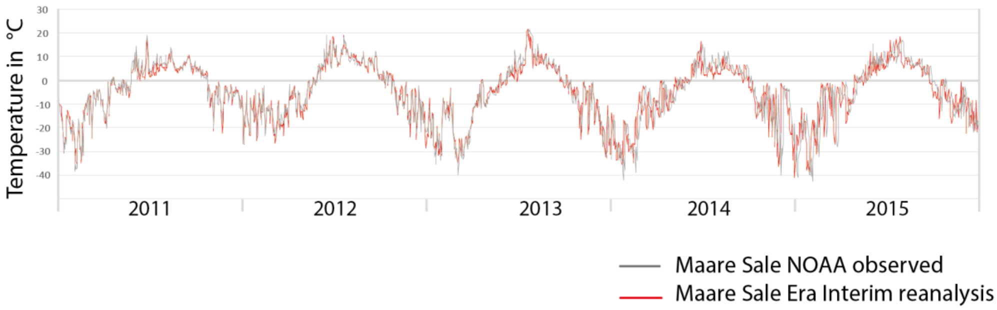

Figure 5-6 Comparison of observed NOAA and reanalysis data from Era Interim temperature in Maare Sale.

Precipitation

As shown in figure 5-7 observed precipitation data downloaded from NOAA contain a high amount of data gaps (29 % of downloaded data, 539 out of 1821 days). The trends of precipitations are similar concerning the available data with a Pearson correlation of r = 0.89, whereas era interim precipitation shows in average higher values. However, a comparison and verification of the monthly accumulated precipitation is difficult. The best year for data coverage occurred in 2012, despite there being a lack of data for the month of May (Figure 5-8). In general, trends of precipitation in 2012 were similar with a correlation coefficient of r = 0.94. Yet, there are large discrepancies in the summer average quantity. The Era Interim accumulated summer rainfall was 274.4 mm and the observed data from NOAA were 218.1 mm (Figure 5-8). However, the winter months show similar precipitation amounts.

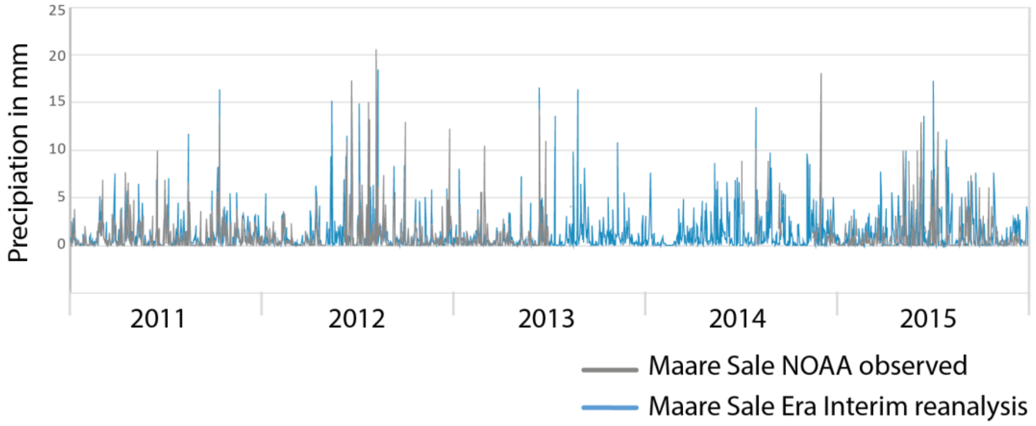

Figure 5-7 Observed daily precipitation compared with reanalysis precipitation data.

5.4 Comparison of Reanalysis Data in Maare Sale and Vaskiny Dachi

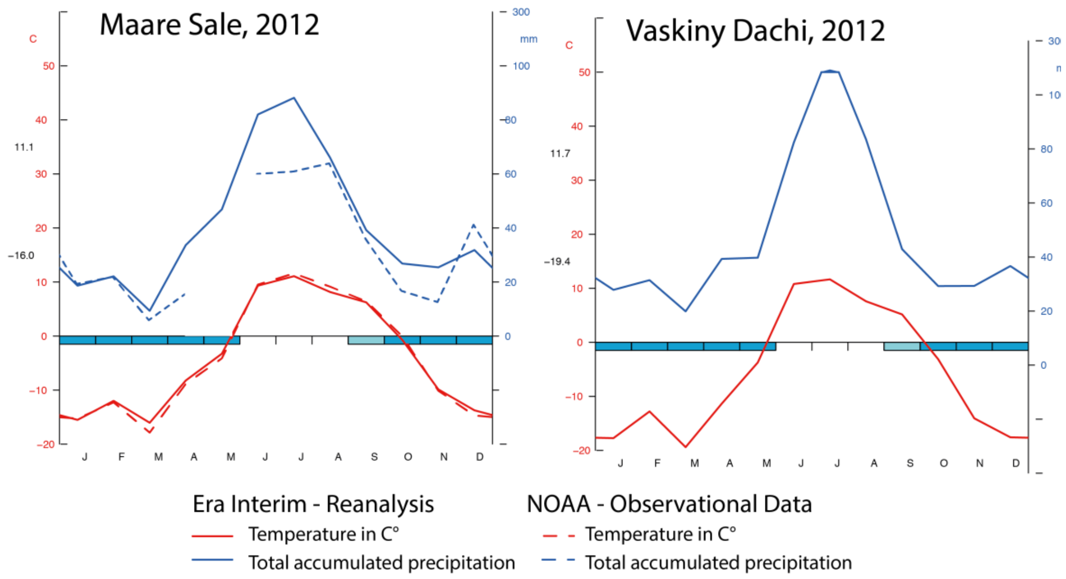

Figure 5-8 Comparison of observational data (dashed line, NOAA) and reanalysis data (Era Interim) in Vaskiny Dachi and Maare Sale displayed in a Walter-Lieth diagram.

Temperature

The Pearson correlation between both data sets of temperature daily means is very high (r = 0.99). Average temperature over the years 2008-2015 in Maare Sale is -5.8°C (± 11.2 °C) and in Vaskiny Dachi -7.58 °C (± 12.8 °C). Vaskiny Dachi is on average 2.41°C (± 1.48°C) colder in the winter months (October to May) and with 0.61°C (± 0.69°C) warmer in the summer months (June to September) compared to Maare Sale.

Precipitation

The Pearson correlation of the monthly accumulated precipitation datasets shows with r = 0.88 a high accordance. Precipitation rates are in general slightly higher in Maare Sale with a yearly total mean precipitation of 509.1 mm in Maare Sale and 497.5 mm in Vaskiny Dachi. Only in the summer months are higher precipitation rates observed in Vaskiny Dachi as seen in figure 5-8.

5.5 Climate Characteristics in Vaskiny Dachi

A summary of the climate characteristic can be seen in table 5.3. The annual mean air temperatures fluctuated considerably from year to year with an average of -7.5°C. The study area is characterized by long severe winters, short summers and a large temperature range between the mean temperature of the coldest and warmest month by an average of 38.6 °C. The coldest months vary between January, February and March with mean temperatures of -2.9 (± 6.9°C), -23.8°C (± 6.6 °C) and -19.07°C (± 6.81°C), respectively. The warmest month is July with a mean temperature of 10.8°C (± 2.5°C). In general, the temperatures show higher fluctuations in winter than in summer (Figure 5-9).

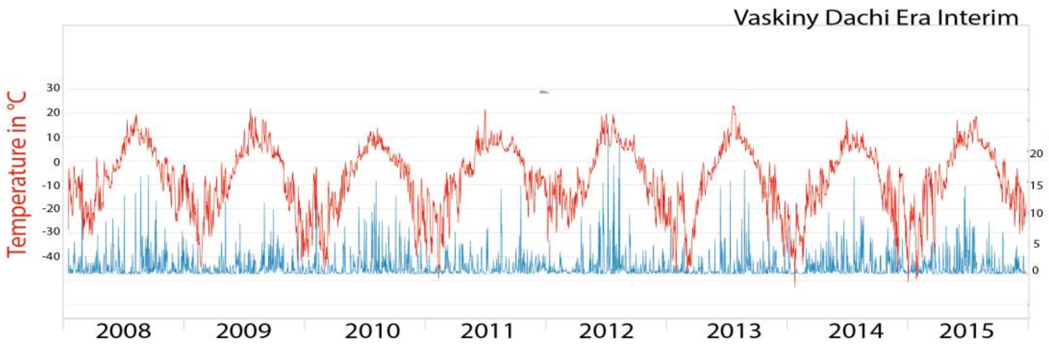

Figure 5-9 Era Interim daily precipitation and daily mean temperature in Vaskiny Dachi

Positive monthly mean temperatures are observed from June to September. The cumulative days over 0 °C vary between 111 days in 2013 and 147 days in 2012 (Table 5-1). The amount of days above 0°C and the thawing index are not correlated to each other (r = 0.3). The thawing index shows a large fluctuation between 704 °C in 2008 and 1059.5 °C in 2012. The differences are much more pronounced in the freezing index with the highest index in 2011 and 2012 (Figure 5-10).

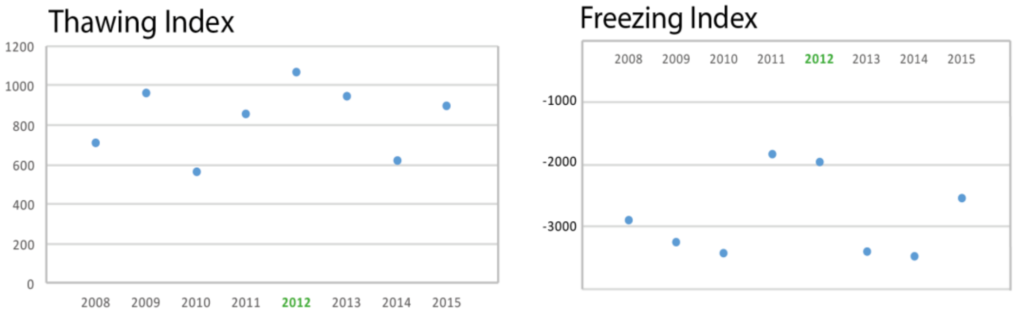

Figure 5-10 Thawing index and freezing index of Vaskiny Dachi in the period from 2008 to 2015 using Era Interim data.

Averaged over the 2008 to 2015 period, 46 % of the yearly amount of precipitation falls as rain (summer monthly average: 51.0 mm, winter monthly average: 28.7 mm). 70% of the total precipitation were light with less than 1mm. Rainfall usually occurs between end of May and end of September. From 2008 to 2015 the rainfall varied between 130.9 mm (± 11.2 mm) in 2011 and 291.5 mm (± 26.05 mm) in 2012 (Figure 5-9). A classification between high (>10 mm) and very high precipitation (>16 mm) was made. As shown in figure 5-11, 26 high (2.7 % of total precipitation) and 5 very high (0.5 % of total precipitation) events were counted within the observed period. They occurred predominantly in summer and the highest density of high precipitation events can be seen in 2012.

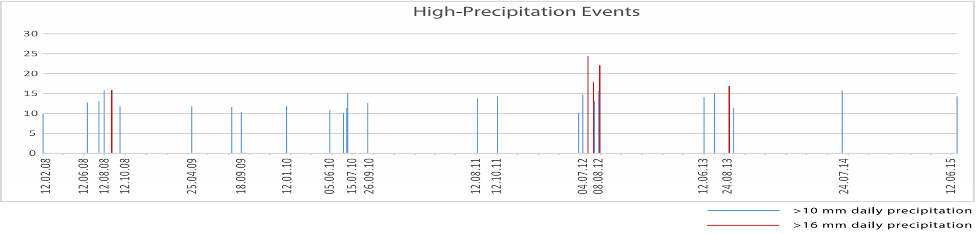

Figure 5-11 High- and very high precipitation events in the period from 2008 to 2015

Table 5-3 Overview of climate characteristics in Vaskiny Dachi for the years 2008-2015 from Era Interim and SSF data. The dates showing the yearly start of the thaw-back/freeze-back of soil. This was determined as the time, were temperatures had been continuously above/below 0°C and where SSF was flagged as thawed/frozen soil.

	Era Interim Annual mean temperature and (°C)	**Era Interim** Mean January temperature and standard deviations (°C)	**Era Interim** Mean July temperature and standard deviations (°C)	**Era Interim** days above 0°C from daily average	**Era Interim** Thawing Index	**Era Interim** Freezing Index	**Era Interim** continous temperatures above 0°C	**ASCAT backscatter** Surface State Flag continously thawed soil
2008	-5.2	-12.3 ± 6.2	12.8 ± 3.3	123	704	-2908.7	8 Jun - 27 Sep	19 Jun - 7 Oct
2009	-9.1	-21.1 ± 6.7	11.6 ± 5.0	137	950	-3276.4	2 Jun - 11 Oct	8 Jun - 13 Oct
2010	-9.6	-20.9 ± 10.1	8.4 ± 40.9	124	552.4	-3455.3	1 Jun - 15 Sep	6 Jun - 23 Sep
2011	-5.2	-22.4 ± 7.4	7.5 ± 2.2	147	844.4	-1857.4	25 May - 10 Oct	2 Jun - 14 Oct
2012	-5.4	-17.7 ± 3.8	11.6 ± 3.4	133	1059.6	-1966.3	26 May - 27 Sep	2 Jun - 1 Oct
2013	-9.4	-28.3 ± 8.0	14.6 ± 5.3	111	937	-3420.4	7 Jun - 22 Sep	7 Jun - 24 Sep
2014	-9.7	-32.7 ± 8.5	7.9 ± 3.4	117	612.6	-3505.1	12 Jun - 3 Oct	12 Jun - 5 Oct
2015	-7.1	-30.9 ± 10.0	12.0 ± 3.8	149	892.1	-2562.7	25 May - 29 Sep	no data

5.5.1 Comparison of Era Interim Temperature and Backscatter / SSF

The backscatter dataset shows a temporal data coverage of 99.3%, which was sufficient for the analysis. The microwave backscatter differs significantly between the seasons, as seen in figure 5-12. The backscatter in summer is higher than in winter due to the dielectric properties of the soil water. Subsequent backscatter decreases can be observed in the period of snow melt. The annual start of snow melt varies between the different years examined. In the years 2008, 2011 and 2013, two events of snowmelt in April and May can be seen (see Appendix A, Fig. A-3).

To evaluate backscatter with Era Interim 2 m temperature data, it is important to consider that the daily mean value was calculated at 12:00 and 00:00 UTC; therefore, this data does not show the min/max values of the day. Era Interim temperature data show reliable results, when compared with SSF (Fig. 5-12). Generally, the accuracy is highest in summer and winter and lowest in transitional periods. However, the start of the freeze cycle coincides better with Era Interim temperatures than the beginning of the thaw cycle.

5.5.2 Evaluation of Climate in 2011/2012

In the following the 2011/2012 will be examined more closely concerning the event of landslides in 2012.

The season is characterized by a short winter. The cold season in 2011 started late compared to the other observed years (Table 5-1). Era Interim temperatures show a change to negative temperatures around the 10 October 2011. With a delay of around four days the backscatter drops and the SSF shows a frozen soil status (~14 October 2011). The winter season is also characterized by higher temperatures with a freezing index of -1966.3°C (Figure 5-10).

As depicted in figure 5-12, one big event of snowmelt starting on the 20 May 2012 can be observed due to a sudden drop of the backscatter. The early start of thawing coincides with positive Era Interim temperatures and sets it apart from the other examined years. The following days mean temperatures are slightly below 0 degrees, while the backscatter data shows a thawing period. This was to be expected as the calculated Era Interim temperature mean does not show the daily maximum temperature. However, the fluctuations between positive and negative temperatures in the start of the thawing cycle are not very well reflected in the SSF. From the 29 May 2012 the SSF shows a state of frozen soil. However, Era Interim already shows temperatures significantly above 0°C. The start of continuous thawed soil in the SSF data starts with the 2 June 2012. In general, the summer temperatures in 2012 were warmer than average, also represented in the second highest thawing index of 1059.5 °C (Figure 5-13).

The change to negative temperature starts on the 27 September 2012. The response to negative temperatures can be seen 5 days later in the SSF. The fluctuations between positive and negative temperatures are very well reflected in the SSF. Continuous temperature below 0°C and a frozen soil were recorded from the 15 October 2012.

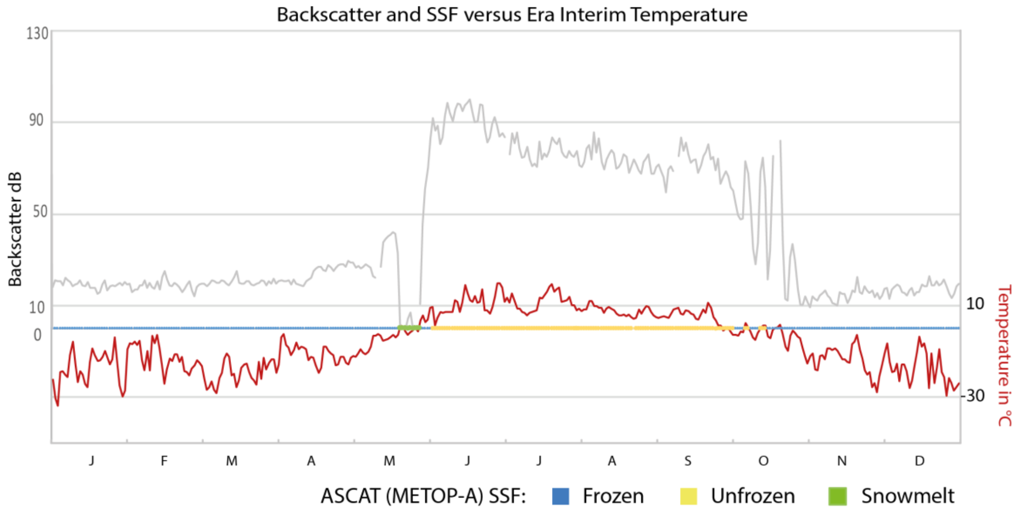

Figure 5-12 Backscatter data ASCAT Metop-A satellite, Vaskiny Dachi, research station and SSF compared with Era Interim air temperatures.

The high mean temperature of -5.2 °C in 2012 coincides with high precipitation rates as seen in figure 5-13. The snowfall in 2011/2012 was 240.5 mm, which in comparison to other years is very high (Figure 5-13). The rainfall from June to September accounts with 291.5 mm for 46% of the mean annual precipitation and is the highest in the observed period. In general, the precipitation below 1 mm accounted for 63 % of the total precipitation. Three very high precipitation events with more than 16 mm per day were recorded in 2012. The highest monthly precipitation was obtained in July with 108 mm, including two high precipitation events on the 04 July 2012 with 24 mm and on the 21 July 2012 with 17.7 mm. Another high precipitation event occurred on the 08.08.2012 with 22.1 mm (Figure 5-11).

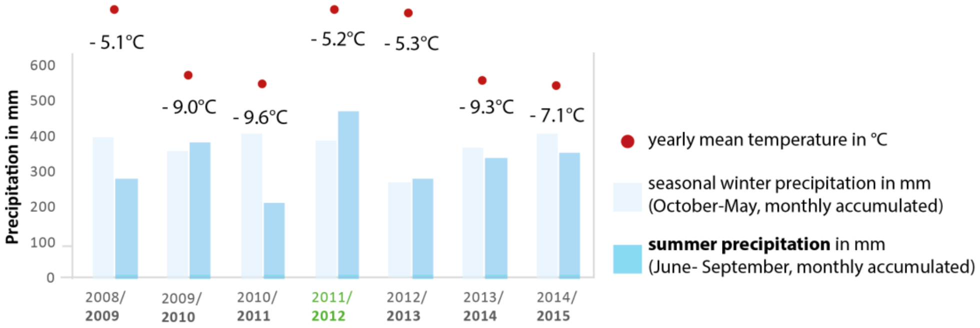

Figure 5-13 Comparison of the seasonal precipitation rates and yearly mean temperatures. 2012 shows a high mean temperature, high winter precipitation and the highest summer precipitation

5.5.3 Analysis of Wind Data

Wind data was plotted in rose diagrams, as seen in figure 5-14 and figure 5-15. The wind speeds were classified according to the Beaufort scale. A differentiation of summer (June to September) and winter season (October to May) was performed to see if the wind has an influence on the orientation of the landslide aspect in terms of either snow accumulation in winter or wave orientation in lakes in the summer season. Observed wind data from NOAA were not available for a comparison.

Comparison of Maare Sale and Vaskiny Dachi

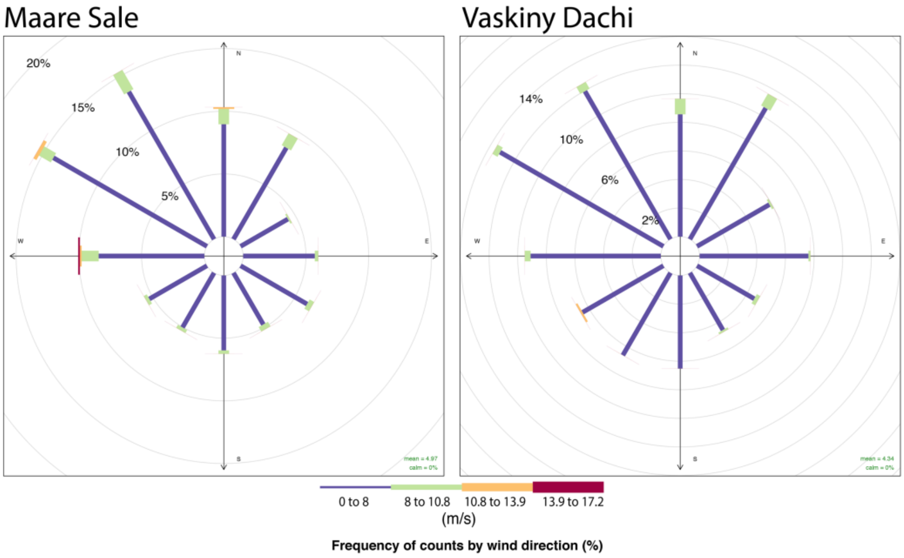

Figure 5-14 Comparison of summer wind roses in Maare Sale (left) and Vaskiny Dachi (right)

The average wind speed of 6.4 m/s in Maare Sale is higher than in Vaskiny Dachi with 5.4 m/s. A comparison of the summer winds (Figure 5-14) shows a more pronounced north western direction in Maare Sale compared to Vaskiny Dachi. Also higher frequencies of Beaufort number 6 and 7 can be observed at Maare Sale.

Wind in Vaskiny Dachi

The study area is characterized predominantly by calmer winds. As seen in figure 5-15 a seasonal variability in the circulation pattern can be observed. In the winter season winds from all directions are common with a preference of south-eastern and south-western winds. The wind speeds can reach up to 16.9 m/s and are on average 0.9 m/s stronger than in the summer season. In general, a higher frequency of Beaufort number 6 and 7 (13.9 m/s – 17.2 m/s) occurred in winter, and the majority of them are south-western winds.

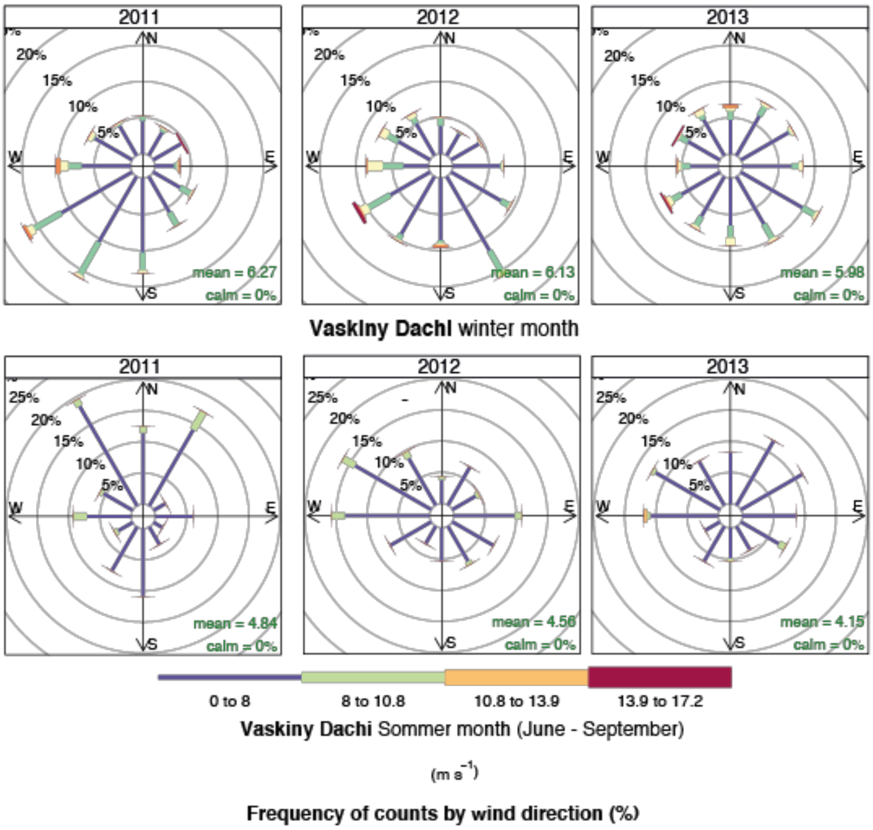

Figure 5-15 Wind rose diagrams show wind direction and wind speed measured in 12 hour intervals. The length of the wind speed bar is proportional to the frequency from the according direction. The classification of wind speed is related to the Beaufort scale with values from 1 to 7. Comparison of the seasonal winds shows a different pattern of winter and summer winds with stronger winds in winter.

In the summer months, winds are also coming from all directions. In contrast to the winter season, the highest frequency occurs from north-western to north-eastern the opposite direction (Figure 5-15). Within this range, the main direction is varying from year to year. The majority of wind speed can be classified into low to moderate wind speeds with up to 97 % of wind measurements. Only a low frequency of higher wind speeds in the range of Beaufort scale 6 to 7 observed; however, these do not show a prevailed direction.

6 Discussion

6.1 Remote Sensing Data

The mapping of disturbances was conducted on the base of high-resolution optical satellite imagery acquired in 2010 (QuickBird) and 2013 (GeoEye-1), which have nearly the same spatial resolution and were therefore, suitable for the change detection. The disturbed area was performed by manual mapping and thus, the calculated area can be differing slightly from user to user. The DEM with a resolution of 12 m was the best available product for the region. For a detailed analysis of the terrain it was too coarse, however, aspect analysis could be performed.

6.2 Evaluation of Reanalysis Data

Reanalysis is a very beneficial tool in climate research, but as with all observation of climate, uncertainties do exist (Dee et al., 2011). Since the accuracy of reanalysis data is not well known in higher latitudes (Lüpkes et al., 2010; Westermann et al., 2015), the thesis aimed to evaluate Era Interim reanalysis data with observational data, ASCAT backscatter and SSF to identify surface conditions.

6.2.1 Evaluation of Observed and Reanalysed Data in Maare Sale

There are several error sources to take into account when comparing observed and reanalysed data. The comparison of the reanalysed grid cell and the observed point location from NOAA poses one error source. The grid cell of Era Interim with a size of 80 km x 80 km is very coarse for the high heterogenic permafrost landscape. Thus, the pixel cell of the coastal station Maare Sale was influenced by around 50 % of ocean and had to be changed to the adjacent pixel (see chapter 4.3.1), resulting in a spatial difference to the meteorological station of around 40 km. Moreover, the Era Interim daily mean temperature does not include the extremes of the minimum and maximum temperatures, unlike observed temperatures, as it was retrieved from 12 hourly steps. To obtain reanalysed temperature time series for future investigations a study of Cornes & Jones (2014) demonstrated that 3 hourly time steps tend to be more reliable. Nevertheless, the study is limited to only one observed climate dataset from the Maare Sale station, where the reliability of data cannot be evaluated with respect to incorrect measurements. Due to this, only a comparison of reanalysis and observed data relative to each other was possible.

Looking at the temperature datasets, the Pearson correlation based on daily means from 2007-2015 is with r = 0.97 very high and the mean deviation of 0.4°C delivers adequate results with respect to the potential error sources described before. The high accordance with measured data is likely, as reanalysed temperature is regularly assimilated from both radiosonde and satellites and the meteorological station itself (Bosilovich, 2013). The comparison of precipitation data was more inaccurate. The observed data set from NOAA contains a high amount of data gaps. The available data show a high Pearson correlation of r =0.88 with reanalysis data, albeit deviations in monthly accumulated precipitation can be seen, especially in the summer months (Figure 5-8). Large uncertainties in precipitation estimates over the Arctic regions have also been observed by previous studies (e.g. Yang et al., 2005). This is caused by sparse observation networks, space-time discontinuities of precipitation data, and underestimation of real precipitation due to gauge undercatch (Screen & Simmonds 2011).

6.2.2 Comparison of Reanalysed Data in Vaskiny Dachi and Maare Sale

The comparison of Era Interim data between the coastal station Maare Sale and the study area in Vaskiny Dachi reflects the seasonal changes of maritime and continental influenced climate. Vaskiny Dachi is around 2.5 °C colder in winter and slightly warmer (0.7°C) in summer. The monthly precipitation is slightly higher in Maare Sale, with some exceptions in the summer month, where higher precipitation rates in Vaskiny Dachi are observed. The climate trends of both locations correlate very well, whereas the Pearson correlation of temperature with r = 0.99 is higher than for precipitation with r = 0.88. The wind data show as expected higher wind speed at the coast with a yearly average wind speed of 6.4 m/s in Maare Sale compared to an average wind speed of 5.4 m/s. The wind direction shows more pronounced north-western summer wind direction at the coast than in Vaskiny Dachi. The climate data differences of both stations demonstrate that it is beneficial to conduct reanalysis in the region. More research should be performed in the future by taking into consideration more meteorological stations and cross-validation studies of other remote sensing products.

6.2.3 Comparison of Surface State Flag and Era Interim Temperature

The SSF data set shows a high accordance with Era Interim temperatures in Vaskiny Dachi as displayed in figure 5-12. This is also supported by other studies which show that the accuracy of ASCAT SSF is over 90% in Siberia and Alaska when evaluated with air and near surface measurements (Heim et al., 2013; Gouttevin et al., 2013).

The datasets reveal that the beginning of the freezing cycle is better reflected with Era Interim temperatures then the start of the thawing cycle. Surprisingly, the beginning of thawed soil in 2012, as seen in figure 5-12, coincides with negative era interim temperatures that are close to 0 degrees. This could be linked to the calculation of the Era Interim daily mean value as discussed in section 6.2.1, which does not reveal the first positive maximum temperatures, where thawing processes are likely to begin. Nevertheless, the expected delay of the frozen soil in response to negative temperatures and a delay of thawing soil to positive temperatures are in general well reflected (see table 5-1). Nevertheless, it has to be considered that the seasonal thaw and freeze back dates can differ from site to site, depending on the respective vegetation complex and on local snow accumulation (Leibman et al., 2015)

6.3 Vulnerability of Study Area

The region is highly susceptible to land cover changes due to high ground ice content, tabular ice deposits, ice wedges and fine-grained sediments in a warming environment (Anismov & Reneva, 2006; Khitun & Rebristaya, 2002; Kumpula et al., 2011). The vulnerability of the study area is also demonstrated by research of Nelson et al. (2001), who created an Arctic hazard map and classified the region under the high risk of thaw-induced settlement (Figure 6-1). In the following this will be discussed with regard to the construction of the railway line and the high occurrence of Retrogressive Thaw Slumps in 2012.

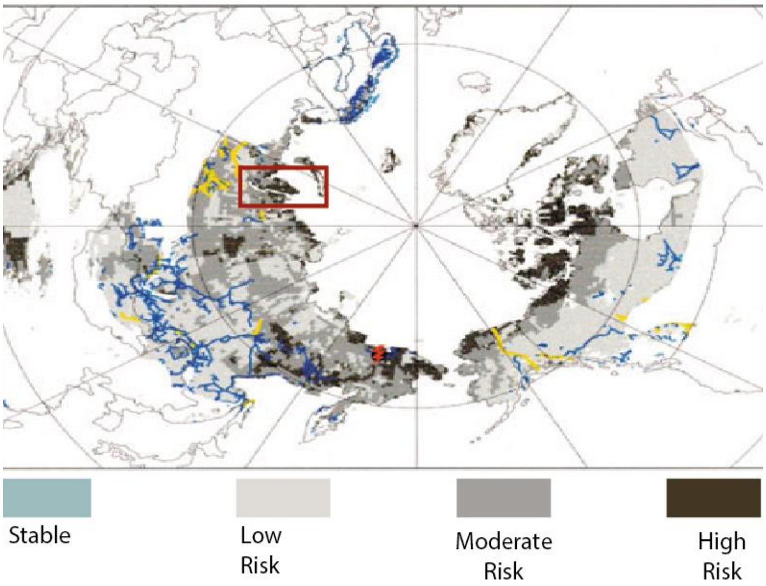

Figure 6-1 Permafrost hazard potential in the Northern Hemisphere, Yamal Peninsula is marked by a red rectangle and shows a high risk of thaw settlement in the area of Vaskiny Dachi, modified after Nelson et al. (2001).

6.3.1 Initiation of Landslides

The study area is characterized by a high level of disturbances from stabilized and active landslides (Gurbakov et al., 2014; Khomutov & Leibman., 2014). By 2010, the satellite image shows that former landslides looked stabilized, overgrown by vegetation. However, the last widespread landslide activity was observed in 2012 by fieldwork (Leibman et al., 2015), triggering several large RTS in forms of thermocirques at the lake margins, but only a few landslides were characterized as active layer detachments (Leibman et al., 2015). The satellite image from 2013 reveals a number of 81 RTS with a total disturbed area of 0.35 km^2 in the study area which covers 266.3 km^2. Comparing it to the landslide event reported in 1989, the disturbance level is considerably lower. In 1989, 400 active layer detachments occurred in an area of 90 km^2 (Leibman et al., 2014). However, in 2012 a remarkably high occurrence of RTS instead of ALD is observed, which shows a high contrast to 1989 levels. It is likely that ice content at the active layer base was not sufficient to trigger ALD (see chapter 2.4). In future studies, reanalysed time series should compare climate data regarding the trigger mechanisms of RTS and ALD which reach back to the 1989 event. This is possible as reanalysis can be obtained from 1979 on.

Aspect Analysis of Landslides

The aspect of cryogenic landslides usually presents a proxy for a number of naturally introduced processes for the initiation of the landslides. An often described parameter is solar insolation, which can result in varying active layer depth with decreased or increased incoming solar radiation (Lacelle et al., 2015; Séjourné et al., 2015; Rudy et al., 2016).

The related rose-diagram shows a high variability of aspects to all directions, with a majority facing to the north and north-west (Figure 5-5). These sites are generally characterized by shallower active layers due to less incoming solar radiation. Nevertheless, the probability of the tabular ground ice being closer to the surface is higher and thus, more prone to melt (Leibman et al., 2015). The accumulated snow on N facing slopes also persist longer which leads to an increased soil moisture in the late season and therefore, the soil is more susceptible for oversaturation and excessive pore pressure (Rudy et al., 2016). A further possibility is the influence of thermal degradation through wind driven wave energy, especially when the lake shore exposes tabular ice. This hypothesis agrees with the direction of summer winds, which originate from the northern direction (Figure 5-15). However, the absence of a predominant wind direction points to a low influence of thermal degradation, but cannot be excluded.

Surprisingly, only a few landslides facing to the south which in many studies were observed as the prevailed direction. These slopes are commonly receiving the highest solar radiation and are characterized by a deeper annual active layer thaw (Lacelle et al., 2010; Rudy et al., 2016; Kharuk et al., 2015).

Summing up, the trigger mechanism of RTS in the study area cannot be clearly determined as a proxy for a prevailing natural process. The high variability of aspects points to a combination of different factors, which might be also influenced by anthropogenic impacts discussed in the next chapters.

Relevance of Climate Influence on Initiation of Landslides

Due to the tectonic inactive region, trigger mechanism as earthquakes can be excluded for landslide occurrence. Therefore, the focus is set to climate impacts, which were analyzed using reanalysed precipitation and air temperature data from Era Interim as well as Metop-A backscatter data and SSF from Naemi et al. (2012). As already mentioned the satellite image of 2010 shows no active landslides. Field studies showed that the occurrence of landslides can be linked to

2012 (Leibman et al., 2015). This is supported by Era Interim time series showing that after two cold years, 2012 is characterized by a very warm and wet year (Figure 5-13).

The winter season of 2011/2012 was the warmest in the observed period, hence, with -1857 the freezing index was very high (Figure 5-10). The continuous thaw season seen in SSF data and Era Interim temperatures started around the 02 June 2012 and set it apart from the other years, where the continuous thawing period started later in time. The summer in 2012 is characterized by high temperatures seen in a high thawing index of 1059.6 compared to the observed period. These climate conditions were also reflected in an increase of ALT (15 % deeper than the average for 1993 – 2011), as seasonal climate change drives the yearly variation of the ALT (Leibman et al., 2015). A strong relationship between thawing index, the duration of thawing period and ALT has been observed by many studies, showing that warmer summers on average cause a deeper active layer (Streletskiy et al., 2015).

Furthermore, the summer rainfall of 498 mm was exceptionally high (Figure 5-13). In total, six precipitation events in July and August were exceeding 10 mm per day, three of which exceeded 16 mm. The importance of intense rainfall events as a driver for the initiation of landslides were also reported in past studies (e.g. Balser et al., 2014; Kokelj et al., 2015). Previous research by Balser et al. (2014) has indicated that beside the magnitude, early seasonal timing of rainfall events might be relevant for the initiation of RTS, as this would accelerate the melting of snow. Nevertheless, in Vaskiny Dachi the high precipitation events occurred in the mid of thaw season. Even though the climate events can be temporally linked to 2012 concerning landslide occurrence, it cannot be ruled out that several landslides also occurred in 2013. For example, saturated soil conditions as a consequence of rainfall events before the onset of freeze-back in 2012 can contribute to ice aggradation in the active layer. This in turn can lead to the development of excess pore-water pressure which has in conjunction with other climate drivers the potential to be released in form of landslides in the following thaw season (Rudy et al., 2016). This is certainly possible as the climate in 2013 is characterized by high summer temperatures and four high precipitation events.

6.3.2 Anthropogenic Impacts

The high-resolution satellite images show the anthropogenic impacts on permafrost soil in the massive gas-producing environment of Central Yamal.

The landscape has been altered by extensive off-road travel and the construction of the railway line for the Bovanenkovo gas field a few kilometers further north (Leibman et al., 2015). Disturbances associated with the construction of the railway line include a wide range of direct impacts - off-road vehicle use, temporary camps/storage areas, quarries and indirect impacts - blowing sand/dust, landslides and changes in topography, hydrology and surface albedo. While the direct impacts are better to detect through optical remote sensing imagery, indirect effects are underrepresented in the study and need further investigation.

The railway line was classified into three different levels of lateral erosion (Figure 5-2). The classification level is reflected in the disturbance area per meter, which increases with higher class of disturbance magnitude. The highest disturbance of construction features can be seen through bridges. After the completion of the construction in 2010 the railway embankment in 2013 seems to be stabilized in most parts due to natural revegetation and maintenance techniques. Parking areas and housings were for the most parts removed and seem to be revegetated. The disturbance level decreased from 2.5 km^2 in 2010 to 1.58 km^2 in 2013. However, new lateral erosion can be seen, especially in the section of the highest disturbance section of M3, showing how vulnerable the region is in regards to anthropogenic impact.

6.4 Relation of Anthropogenic and Natural Impacts

The change detection study revealed that human-induced disturbances exceed natural disturbances by a factor of at least five in 2013, excluding off-road disturbances. The study is led by the hypothesis whether the construction of the railway line also increases the probability of landslides occurrence. In the following this will be analyzed through an examination of the landslide distribution within the study area. A summary of short-term changes of the relationship between natural and anthropogenic impact can be seen also in figure 6-2. The landslide pattern is not uniform over space, as seen in the density map. The occurrence depends highly on lake distribution, as well as the topography and the lithology of the soil (Leibman et al., 2015).

The highest landslide density can particularly be observed in flat areas, especially on floodplains and in the vicinity of the railway line. Flat areas allowed higher lateral disturbance driven by gravity, than hilly areas, where less disturbance was observed. The magnitude of the disturbance level from the railway disturbance is reflected in the surrounded lake density. Sections with higher disturbances are in most cases also encompassed by a higher number of thermokarst lakes. The high occurrence of lakes adjacent to the highly disturbed section might also emphasize that the area is more prone to permafrost degradation

A study of Yu et al. (2015) analyzed land cover changes due to oil and gas exploration in the southern region of Yamal with most direct impacts observed within 100 m distance from the industrial disturbance sources. In reference to the 100 m threshold, eight landslides adjacent to the railway were detected. The bare surfaces caused by construction work are more prone to external climate factors. Whether these landslides occurred simultaneously to other landslides in terms of climate amplification or were triggered by changes in topography is of question. Future work could make use of the model by Nitze & Grosse (2016), who created Landsat time series stacks to gain a better understanding of the spatio-temporal dynamics of landslides.

The indirect impacts of the railway line were analyzed using the kernel density distribution of RTS, since changes in hydrological processes can occur several kilometers away from the physical footprint of the structure (Jin et al., 2008; Gill et al., 2014; Raynolds et al., 2014). The attention was based on processes, which can increase ALT. With an increase of ALT more space to capture water is produced, and thus, the potential of mass wasting processes is more likely (Kharuk et al., 2015). The main focus of the study is presented by two hotspots of RTS occurrence, both located in the flat areas of the study area. The key area A shows the highest kernel density of landslide distribution (n = 33) and is also highly affected by high-level anthropogenic impacts, whereas key area B is unaffected by anthropogenic impact, and shows a less number of RTS (n = 18), which are more dispersed. This demonstrates that RTS has to be primary considered as a natural phenomenon, as they occurred in the whole study area independent of human impact. However, it also underlines the difficulty to quantify how far reaching anthropogenic impacts on landslide occurrences are.

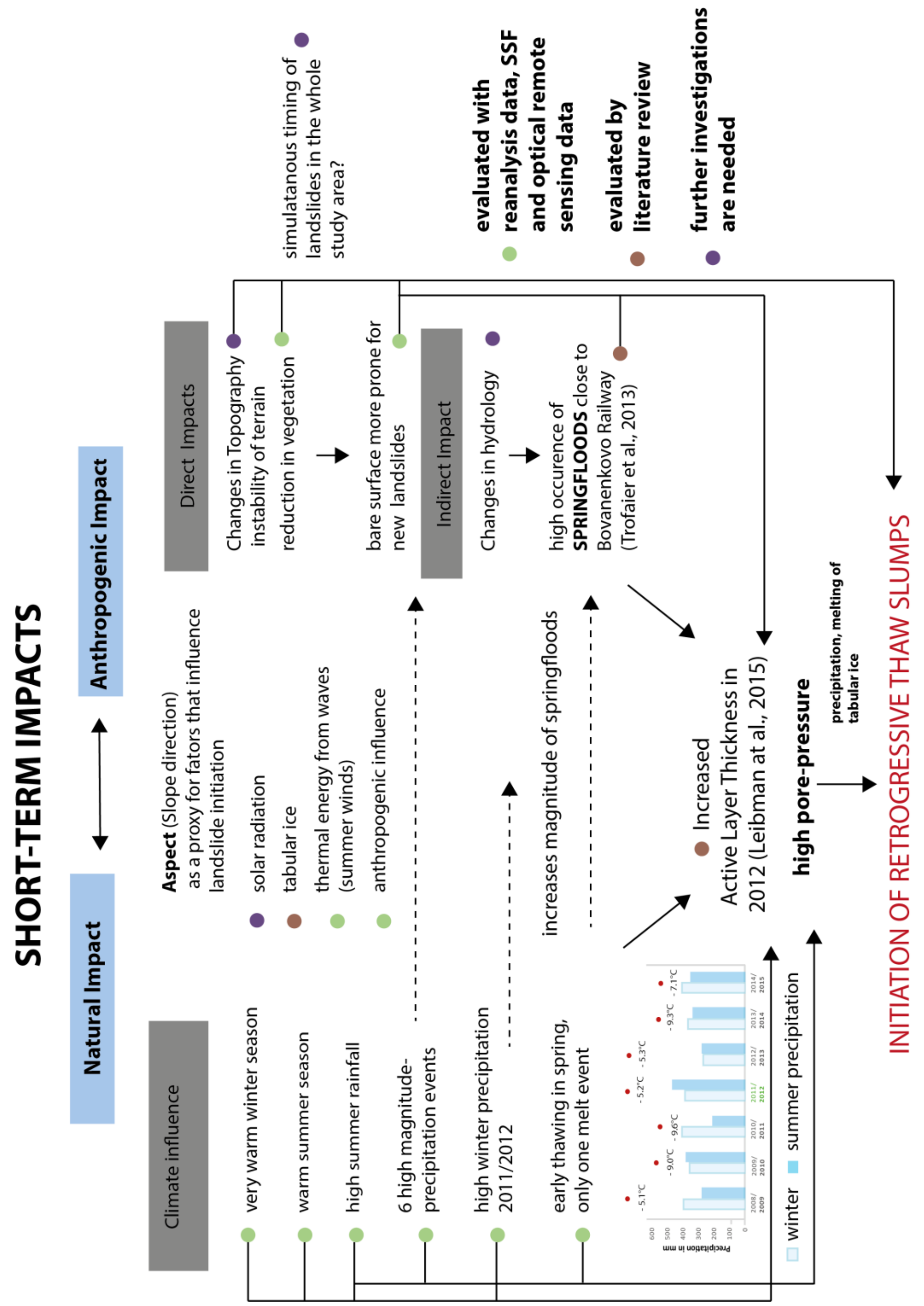

Figure 6-2 Summary of the discussed short-term impacts, which can influence the initiation of retrogressive thaw slumps.

An increase of ALT in areas along linear infrastructure was noted by Zakharova et al. (2009). They demonstrate that infrastructure creates a physical barrier in the landscape, which modifies the hydrology and favors the formation of new primary drain networks. In the study area RTS occurrence might be also amplified by the high level of off-road tracks used for railway construction. Off-road tracks can be particularly observed in the vicinity of the railway and sometimes very close to the lake margins. The tracks alter the surface and subsurface conditions due to a decreased albedo caused by the removal of vegetation and water logging processes. These changes lead to surfaces which absorb more heat and thus, have an influence of increasing the ALT (Gill et al., 2014).

The most important observation in regards to this study was made by Trofaier et al. (2013), who analyzed seasonal lake inundations at larger scales in Yamal. These changes in lake water extents are associated with the effects of spring floods and contribute to a warming ground, rapid snow removal and thus, an acceleration of the active layer development (Koklj & Burn, 2005). Lake inundations could be in particular observed along the Obskaya-Bovanenkovo railway in July and August and were therefore, discussed as effects influenced by anthropogenic impacts (Figure 6-3).

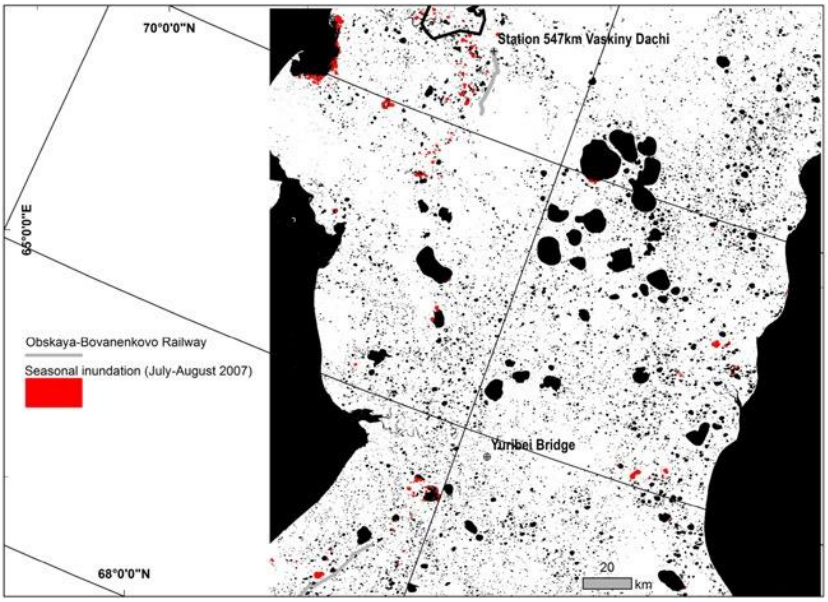

Figure 6-3 The seasonal changes of water extent for July –August 2007 are depicted in red. The key area Vaskiny Dachi shows the highest density of seasonal changes in water extent, especially to the west of the Bovanenkovo Railway (Trofaier et al., 2013) In this area also the highest density of landslides was found (see figure 5-2).

In conjunction with the high winter precipitation in 2011/2012 with only one melt event (Figure 5-12), a high lake water extent can be assumed, which likely contributed to the deepening of the active layer at the lake margins. Special attention needs to be given to the area of the highest density of observed lake water extents in the west of the Bovanenkovo railway line around Vaskiny Dachi (Fig. 6-3), which coincides with the area of the highest density of RTS (Figure 5-2). This area is also located close to a floodplain, which enhance the effect of lake inundation and hydrology changes through the railway line and thus, amplifies climate drivers to trigger RTS. Additional investigations will be necessary to determine the hydrologic conditions and active layer dynamics in the area close to infrastructure features.

6.5 Indirect Effects and Relevance of Disturbances

In the previous chapter, central effects of the railway line were pointed out, however, there are more indirect impacts to mention.
The satellite image from 2013 shows a progressed state of landslides assumed to be in most cases a year after initiation. Field investigations showed that RTS increased twofold from their initial size after the first year. They reported that the retreat rate is on average around 15 m/year and can reach up to 25 - 30 m/year (Khomutov et al., 2016). Thaw slumps will continue to retreat until the ground ice supply is exhausted (Lantuit & Pollard, 2008; Lacelle et al., 2015).

Studies of Lantz et al. (2009) suggest that these exposed sites may act as highly productive seed sources and provide opportunities for rapid colonization. As seen in pictures from the expedition in 2013, taken by A. Bartsch and also seen in the 2013 satellite image, pioneer plants occupied the disturbed surfaces after one year of inactivity. These plants are taller than the surrounded undisturbed terrain (Leibman et al., 1998). Expansion of tall vegetation can result in surface albedo decline during periods of snow cover, as the vegetation absorbs radiation otherwise reflected by snow (Loranty et al., 2011; Khitun & Rebristaya, 2012). In turn, the changes in surface albedo will give a positive feedback to climate warming. Greening trends due to climate and anthropogenic factors have been already observed in Yamal by satellite time series (Lantz et al., 2008, 2009; Walker et al., 2009; Zeng et al., 2013). Furthermore, thaw slumps can have discernible effects on lake-water chemistry (Zeng et al., 2013). Degrading permafrost releases soluble materials, which can modify water chemistry of lakes (Kokelj et al., 2009; Séjourné et al., 2015; Dvornikov et al., 2015).

6.6 Future Development of Human and Natural Impacts

As in the past sections discussed, climate warming and gas development are the major drivers in the study area, which alter the landscape with regard to vegetation, topography and hydrology (Yu et al., 2015).

Future projections of climate models show a remarkable degree of warming in the Arctic at rates double that of lower latitudes, also termed as the Arctic Amplification (e.g., Serreze et al., 2009; IPCC, 2013, Cohen et al., 2014). The forecast of these climate scenarios show an increase of mean air temperatures from 7°C to 11° by the end of the 21st century (Kharuk et al., 2016). Increased temperatures are also correlating with permafrost warming (Kharuk et al.,2016). If the permafrost temperature gets warmer, the shear and normal stresses of the frozen ground are decreasing, leading to less ice-bonding and thus, to an increased likelihood of landslide initiation (Kharuk et al., 2016). Romanovsky et al. (2010) showed that during the last four decades the permafrost temperatures increased to 0.3°C – 2 C° in Siberia. Moreover, global circulation models also forecast significant increases in extreme rainfall events in the Arctic (Walsh et al., 2011). Due to this the frequency and magnitude of cryogenic, landslides will be expected to increase in the future (Kharuk et al., 2016; Lantz and Kokely, 2008; Shan et al., 2015). Lantz et al., (2009) pointed out that these disturbances have a stronger and more immediate impact on Arctic ecosystems than increasing temperatures by itself. Although landslide disturbances are relatively small, their frequency as well as the aerial extents, are increasing and alter vegetation (Lantz & Kokelj, 2008; Lantz et al., 2009).

Along with climate warming, the Russian sector of the Arctic will continue to play a leading role in the extraction of gas and oil, especially at the Yamal Peninsula (Kampula et al., 2012). The future gas exploration will be carried out in an environment with shorter periods of frozen soil. Thus, consequences of vehicular traffic in winter are difficult to predict. Although the railway line might decrease the use of off-road tracks in future, it enables the access for more anthropogenic activities and transportation across Yamal.

7 Conclusion

The results of this study are important to deduce information of natural and anthropogenic impacts of permafrost degradation in the future with respect to projected global warming. The change detection revealed that human-induced disturbances exceed natural disturbances by a factor of at least five in 2013. The mapped lateral erosion of the Bovanenkovo railway line shows different levels of disturbance extent from 2010 to 2013. The highest lateral disturbance occurs where the railway line passes flat areas and lakes and where bridges cross streams. In 2013, most parts seem to be stabilized through natural revegetation and stabilization techniques with a decrease of 38 % compared to 2010. However, active thaw settlement along the railway line can be observed, which demonstrate the vulnerability of permafrost soil to human impacts and underlines the importance of regular maintenance. In addition, a number of 81 active retrogressive thaw slumps were detected in the satellite image of 2013, mostly located in flat areas. In contrast to other studies, solar insolation as a trigger mechanism rather plays a minor role, since the majority of aspects are facing NW and N. The aspect of RTS in the study area cannot be clearly determined as a proxy for a prevailing natural process. The high variability of aspects points to a combination of different factors, which might be also influenced by anthropogenic impacts. A better understanding of the climate drivers for the initiation of RTS were gained with reanalysis, backscatter and SSF data. The evaluation of data shows highest accuracy of reanalysis data with temperature data. Precipitation data show same trends but differ in the monthly accumulated precipitation, especially in the summer months. A further important finding is that Era interim reanalysis data reflects the maritime and continental climate in terms of wind, temperature and precipitation very well. It underlines that reanalysis is a beneficial and powerful tool to access climate data in remote areas. However, future research should make more use of cross validation studies with other remote sensing products and meteorological stations.

The climate event is characterized by a mild winter (high freezing index), high winter precipitation, early snow melt, warm summer temperatures (high thawing index) and six high precipitation events exceeding 10 mm with respect to the observed period. These climatic factors lead to an increase of the seasonal active layer depth as well as an increase in pore pressure which resulted in the triggering of RTS.

Although cryogenic landslides appear to be a natural phenomenon in the study area, major anthropogenic impacts seem to contribute to these changes. One hotspot with the highest density of RTS is located in the direct vicinity to the railway line. The bare surfaces caused by railway construction are 1) more exposed to external climate factors, 2) unstable through reduced vegetation cover as well as 3) changes in topography and therefore, increased by the probability of landslide occurrences. Considering indirect impacts at larger scales in terms of several kilometers it is argued that changes in hydrology caused by the railway line can lead to increased lake inundation as observed in the study of Trofaier et al (2013). This in turn might have increased the ALT at the lake margins, which again amplifies the potential of RTS occurrence. However, these findings must be interpreted with care and do not automatically reflect effects of the railway line. In conjunction with projected global warming and future gas exploration, the region will experience significant erosion rates, which will have implications on permafrost dynamics and the surface energy budgets in the study region.

Bibliography

Anthony, K. W., Zimov, S. A., Grosse, G., Jones, M. C., Anthony, P. M., Chapin III, F. S., Finlay, J.C., Mack, M.C., Davydov, S., Frenzel, P. & Frolking, S. (2014). A shift of thermokarst lakes from carbon sources to sinks during the Holocene epoch. *Nature*, *511*(7510), 452-456.

AMAP, A. (2011). assessment 2011: mercury in the Arctic. *Arctic Monitoring and Assessment Programme (AMAP), Oslo, Norway*, *193*.

Anisimov, O., & Reneva, S. (2006). Permafrost and changing climate: The Russian perspective. *AMBIO: A Journal of the Human Environment*, *35*(4), 169-175.

Anisimov, O. A. (2007). Potential feedback of thawing permafrost to the global climate system through methane emission. *Environmental Research Letters*, *2*(4), 045016.

Balser, A. W., Jones, J. B., & Gens, R. (2014). Timing of retrogressive thaw slump initiation in the Noatak Basin, northwest Alaska, USA. *Journal of Geophysical Research: Earth Surface*, *119*(5), 1106-1120.

Bartsch, A., Sabel, D., Wagner, W., & Park, S. E. (2011, July). Considerations for derivation and use of soil moisture data from active microwave satellites at high latitudes. In *Geoscience and Remote Sensing Symposium (IGARSS), 2011 IEEE International* 3132-3135.

Berrisford, P., Kållberg, P., Kobayashi, S., Dee, D., Uppala, S., Simmons, A. J., Poli, P. & Sato, H. (2011). Atmospheric conservation properties in ERA-Interim. *Quarterly Journal of the Royal Meteorological Society*, *137*(659), 1381-1399.

Bosilovich, M. G. (2013). Regional climate and variability of NASA MERRA and recent reanalyses: US summertime precipitation and temperature. *Journal of Applied Meteorology and Climatology*, *52*(8), 1939-1951.

Bromwich, D. H., Fogt, R. L., Hodges, K. I., & Walsh, J. E. (2007). A tropospheric assessment of the ERA-40, NCEP, and JRA-25 global reanalyses in the polar regions. *Journal of Geophysical Research: Atmospheres*, *112*(D10).

Burn, C. R., & Zhang, Y. (2009). Permafrost and climate change at Herschel Island (Qikiqtaruq), Yukon Territory, Canada. *Journal of Geophysical Research: Earth Surface*, *114*(F2).

Cornes, R., & Jones, P. (2014, May). Assessing the reliability of trends in extremes of surface temperature across Europe in the ERA-Interim reanalysis dataset. In *EGU General Assembly Conference Abstracts* (Vol. 16, p. 15302).

Cohen, J., Screen, J. A., Furtado, J. C., Barlow, M., Whittleston, D., Coumou, D., ... & Jones, J. (2014). Recent Arctic amplification and extreme mid-latitude weather. *Nature Geoscience*, *7*(9), 627-637.

Dee, D. P., Uppala, S. M., Simmons, A. J., Berrisford, P., Poli, P., Kobayashi, S., Andrae, U., Balmaseda, M. A., Balsamo, G., Bauer, P., Bechtold, P., Beljaars, A. C. M., van de Berg, L., Bidlot, J., Bormann, N., Delsol, C., Dragani, R., Fuentes, M., Geer, A. J., Haimberger, L., Healy, S. B., Hersbach, H., Hólm, E. V., Isaksen, L., Sanz, B. M., Morcrette, J.-J., Park, B.-K., Peubey, C., de Rosnay, P., Tavolato, C., Thépaut, J.-N. and Vitart, F. (2011), The ERA-Interim reanalysis: configuration and performance of the data assimilation system. *Quarterly Journal of the royal meteorological society*, 137: 553–597.

De Jeu, R. A. M., Wagner, W., Holmes, T. R. H., Dolman, A. J., Van De Giesen, N. C., & Friesen, J. (2008). Global soil moisture patterns observed by space borne microwave radiometers and scatterometers. *Surveys in Geophysics*, *29*(4-5), 399-420.

Duguay, C. R., Zhang, T., Leverington, D. W., & Romanovsky, V. E. (2005). Satellite remote sensing of permafrost and seasonally frozen ground. *Remote sensing in northern hydrology: measuring environmental change*, 91-118.

Dvornikov, Y., Khomutov, A., Mullanurov, D., Ermokhina, K., Gubarkov, A., & Leibman, M. (2015). GIS and field data based modelling of snow water equivalent in shrub tundra. *Fennia*, *193*(1), 53-65.

Dvornikov, Y., Leibman, M., Heim, B., Bartsch, A., Herzschuh, U., Khomutov, A., Gubarkov, A., Mikhaylova M., Mullanurov, D., Widhalm, B. Skorospekhova, T. & Mikhaylova, M. (2016). Colored dissolved organic matter in thermokarst lakes of Yamal peninsula: sources, annual variations and connection to lake and catchment properties. *ICOP2016*, Potsdam, 20 June 2016 - 24 June 2016

Dvornikov, Y., Leibmann, M., Heim, B., Bartsch, A., Haas, A., Khomutov, A., ... & Skorospekhova, T. (2016a). Geodatabase and WebGIS project for long-term permafrost monitoring at the Vaskiny Dachi research station, Yamal, Russia. *Polarforschung*, *85*(2), 107-115.

Forbes, B. C. (1997). Tundra disturbance studies IV. Species establishment on anthropogenic primary surfaces, Yamal peninsula, northwest Siberia, Russia 1. *Polar Geography*. 21, 79-100.

Forbes, B. C. (1999). Land use and climate change on the Yamal Peninsula of north-west Siberia: some ecological and socio-economic implications. *Polar Research*, *18*(2), 367-373.

Forbes, B. C., Ebersole, J. J., & Strandberg, B. (2001). Anthropogenic disturbance and patch dynamics in circumpolar arctic ecosystems. *Conservation Biology*, *15*(4), 954-969.

Forbes, B. C., Stammler, F., Kumpula, T., Meschtyb, N., Pajunen, A., & Kaarlejärvi, E. (2009). High resilience in the Yamal-Nenets social–ecological system, West Siberian Arctic, Russia. *Proceedings of the National Academy of Sciences*, *106*(52), 22041-22048.

Forman, S. L., Ingólfsson, O., Gataullin, V., Manley, W., & Lokrantz, H. (2002). Late Quaternary stratigraphy, glacial limits, and paleoenvironments of the Marresale area, western Yamal Peninsula, Russia. *Quaternary Research*, *57*(3), 355-370.

Frauenfeld, O. W., Zhang, T., & Mccreight, J. L. (2007). Northern hemisphere freezing/thawing index variations over the twentieth century. *International Journal of Climatology*, *27*(1), 47-63.

French, H.M. (2007), *The Periglacial Environment*, Third ed., John Wiley and Sons Ltd, Chichester, UK.

French, H., & Shur, Y. (2010). The principles of cryostratigraphy. *Earth-Science Reviews*, *101*(3), 190-206.

Fritz, M., Wetterich, S., Meyer, H., Schirrmeister, L., Lantuit, H., & Pollard, W. H. (2011). Origin and characteristics of massive ground ice on Herschel Island (western Canadian Arctic) as revealed by stable water isotope and hydrochemical signatures. *Permafrost and Periglacial Processes*, *22*(1), 26-38.

Gill, H. K., Lantz, T. C., O'Neill, B., & Kokelj, S. V. (2014). Cumulative impacts and feedbacks of a gravel road on shrub tundra ecosystems in the Peel Plateau, Northwest Territories, Canada. *Arctic, Antarctic, and Alpine Research*, *46*(4), 947-961.

Gouttevin, I., Bartsch, A., Krinner, G., & Naeimi, V. (2013). A comparison between remotely-sensed and modelled surface soil moisture (and frozen status) at high latitudes. *HESSD*, *10*(EPFL-ARTICLE-188272), 11241-11291.

Grosse, G., Romanovsky, V., Jorgenson, T., Anthony, K. W., Brown, J., & Overduin, P. P. (2011). Vulnerability and Feedbacks of Permafrost to Climate Change. *EOS Transactions*, *92*, 73-74.

Grosse, G., Goetz, S., McGuire, A. D., Romanovsky, V. E., & Schuur, E. A. (2016). Changing permafrost in a warming world and feedbacks to the Earth system. *Environmental Research Letters*, *11*(4), 040201.

Gubarkov, A., Leibman, M., & Andreeva, M. (2013). Cryogenic Landslides in Paragenetic Complexes of Slope and Channel Processes in the Central Yamal Peninsula. *Landslides in Cold Regions in the Context of Climate Change*, 291.

Heim, B., Bartsch, A., Elger, K., Duguay, C., & Seifert, F. M. (2013). User Interaction within the Framework of ESA DUE Permafrost: a Circumpolar Remote Sensing Service for Permafrost. In *(Earth Observation and Cryosphere Science; SP-712)* (No. SP-712, pp. 1-8). ESA Communications.

Hollesen, J., Matthiesen, H., Møller, A. B., & Elberling, B. (2015). Permafrost thawing in organic Arctic soils accelerated by ground heat production. *Nature Climate Change*, *5*(6), 574-578.

Jin, H. J., Yu, Q. H., Wang, S. L., & Lü, L. Z. (2008). Changes in permafrost environments along the Qinghai–Tibet engineering corridor induced by anthropogenic activities and climate warming. *Cold Regions Science and Technology*, *53*(3), 317-333.

Kharuk, V. I., Shushpanov, A. S., Im, S. T., & Ranson, K. J. (2016). Climate-induced landsliding within the larch dominant permafrost zone of central Siberia. *Environmental Research Letters*, *11*(4), 045004.

Khitun, O., & Rebristaya, O. (2002). Anthropogenic impacts on habitat structure and species richness in the West Siberian Arctic. Wilderness in the circumpolar North: searching for compatibility in ecological, trational, and ecotourism values. PMRS-P-26, 85-95.

Khitun, O., Ermokhina, K., Czernyadjeva, I., Leibman, M., & Khomutov, A. (2014). Floristic complexes on landslides of different age in Central Yamal, West Siberian Low Arctic, Russia. *Fennia-International Journal of Geography*, *193*(1), 31-52.

Khomutov, A., & Leibman, M. (2014). Assessment of Landsliding Hazard in Typical Tundra of Central Yamal, Russia. In *Landslide Science for a Safer Geoenvironment*, *Springer International Publishing,* 487-492.

Khomutov, A., Dvornikov, Y., Gubarkov, A., & Mullanurov, D. (2016, April). Activation of thermal denudation under recent climatic fluctuations, Central Yamal, Russia. In *EGU General Assembly Conference Abstracts*, Vol. 18, 311.

Kimball, J. S., McDonald, K. C., Keyser, A. R., Frolking, S., & Running, S. W. (2001). Application of the NASA scatterometer (NSCAT) for determining the daily frozen and nonfrozen landscape of Alaska. *Remote Sensing of Environment*, *75*(1), 113-126.

Kokelj, S. V., & Burn, C. R. (2005). Geochemistry of the active layer and near-surface permafrost, Mackenzie delta region, Northwest Territories, Canada. *Canadian Journal of Earth Sciences*, *42*(1), 37-48.

Kokelj, S. V., Zajdlik, B., & Thompson, M. S. (2009). The impacts of thawing permafrost on the chemistry of lakes across the subarctic boreal-tundra transition, Mackenzie Delta region, Canada. *Permafrost and Periglacial Processes*, *20*(2), 185-199.

Kokelj, S. V., & Jorgenson, M. T. (2013). Advances in thermokarst research. *Permafrost and Periglacial Processes*, *24*(2), 108-119.

Kokelj, S. V., Tunnicliffe, J., Lacelle, D., Lantz, T. C., Chin, K. S., & Fraser, R. (2015). Increased precipitation drives mega slump development and destabilization of ice-rich permafrost terrain, northwestern Canada. *Global and Planetary Change*, *129*, 56-68.

Kokelj, S. V., Lantz, T. C., Tunnicliffe, J., Segal, R., & Lacelle, D. (2017). Climate-driven thaw of permafrost preserved glacial landscapes, northwestern Canada. *Geology*, *45*(4), 371-374.

Kumpula, T., Forbes, B. C., & Stammler, F. (2006). Combining data from satellite images and reindeer herders in arctic petroleum development: the case of Yamal, West Siberia. *Nordia Geographical Publications*, *35*(2), 17-30.

Lacelle, D., Bjornson, J., & Lauriol, B. (2010). Climatic and geomorphic factors affecting contemporary (1950–2004) activity of retrogressive thaw slumps on the Aklavik Plateau, Richardson Mountains, NWT, Canada. *Permafrost and Periglacial Processes*, *21*(1), 1-15.

Lacelle, D., Brooker, A., Fraser, R. H., & Kokelj, S. V. (2015). Distribution and growth of thaw slumps in the Richardson Mountains–Peel Plateau region, northwestern Canada. *Geomorphology*, *235*, 40-51.

Lantuit, H., & Pollard, W. H. (2008). Fifty years of coastal erosion and retrogressive thaw slump activity on Herschel Island, southern Beaufort Sea, Yukon Territory, Canada. *Geomorphology*, *95*(1), 84-102.

Lantz, T. C., & Kokelj, S. V. (2008). Increasing rates of retrogressive thaw slump activity in the Mackenzie Delta region, NWT, Canada. *Geophysical Research Letters*, *35*(6).

Lantz, T. C., Kokelj, S. V., Gergel, S. E., & HENRY, G. H. (2009). Relative impacts of disturbance and temperature: persistent changes in microenvironment and vegetation in retrogressive thaw slumps. *Global Change Biology*, *15*(7), 1664-1675.

Leibman, M. O., Hubberten, H. W., Lein, A. Y., Streletskaya, I. D., & Vanshtein, B. G. (2003). Tabular ground ice origin: cryolithological and isotope-geochemical study. In *Permafrost: proceedings of the 8th International Conference on Permafrost, 21-25 July 2003, Zurich, Switzerland/ed. Vol. 1*, 645-650.

Leibman, M. O., Epstein, H. E., Khomutov, A. V., Moskalenko, N. G., & Walker, D. A. (2008). Relation of active layer depth to vegetation on the Central Yamal Peninsula, Russia. In *Extended abstracts of the 9th international conference on permafrost* (pp. 177-178).

Leibman, M., Khomutov, A., Gubarkov, A., Mullanurov, D., & Dvornikov, Y. (2015). The research station" Vaskiny Dachi", Central Yamal, West Siberia, Russia–a review of 25 years of permafrost studies. *Fennia*, *193*(1), 3-30.

Loranty, M. M., Goetz, S. J., & Beck, P. S. (2011). Tundra vegetation effects on pan-Arctic albedo. *Environmental Research Letters*, *6*(2), 024014.

Lupascu, M., Welker, J. M., Seibt, U., Maseyk, K., Xu, X., & Czimczik, C. I. (2014). High Arctic wetting reduces permafrost carbon feedbacks to climate warming. *Nature Climate Change*, *4*(1), 51-55.

Lüpkes, C., Vihma, T., Jakobson, E., König-Langlo, G., & Tetzlaff, A. (2010). Meteorological observations from ship cruises during summer to the central Arctic: A comparison with reanalysis data. *Geophysical Research Letters*, *37*(9).

Mazhitova, G., Karstkarel, N., Oberman, N., Romanovsky, V., & Kuhry, P. (2004). Permafrost and infrastructure in the Usa Basin (Northeast European Russia): Possible impacts of global warming. *AMBIO: A Journal of the Human Environment*, *33*(6), 289-294.

Melnikov, E. S., Leibman, M. O., Moskalenko, N. G., & Vasiliev, A. A. (2004). Active-layer monitoring in the cryolithozone of West Siberia. *Polar Geography*, *28*(4), 267-285.

Moorman, B. J. (1998). *The development and preservation of tabular massive ground ice in permafrost regions* (Doctoral dissertation, Carleton University Ottawa).

Naeimi, V., Paulik, C., Bartsch, A., Wagner, W., Kidd, R., Park, S. E., Elger, K. & Boike, J. (2012). ASCAT Surface State Flag (SSF): Extracting information on surface freeze/thaw conditions from backscatter data using an empirical threshold-analysis algorithm. *IEEE Transactions on Geoscience and Remote Sensing*, *50*(7), 2566-2582.

Natali, S. M., Schuur, E. A., Webb, E. E., Pries, C. E. H., & Crummer, K. G. (2014). Permafrost degradation stimulates carbon loss from experimentally warmed tundra. *Ecology*, *95*(3), 602-608.

Nelson, F. E., Anisimov, O. A., & Shiklomanov, N. I. (2001). Subsidence risk from thawing permafrost. *Nature*, *410*(6831), 889-890.

Nitze, I., & Grosse, G. (2016). Detection of landscape dynamics in the Arctic Lena Delta with temporally dense Landsat time-series stacks. *Remote Sensing of Environment*, *181*, 27-41.

Okabe, A., Satoh, T., & Sugihara, K. (2009). A kernel density estimation method for networks, its computational method and a GIS-based tool. *International Journal of Geographical Information Science*, *23*(1), 7-32.

Park, S. E., Bartsch, A., Sabel, D., Wagner, W., Naeimi, V., & Yamaguchi, Y. (2011). Monitoring freeze/thaw cycles using ENVISAT ASAR Global Mode. *Remote Sensing of Environment*, *115*(12), 3457-3467.

Park, H., Kim, Y., & Kimball, J. S. (2016). Widespread permafrost vulnerability and soil active layer increases over the high northern latitudes inferred from satellite remote sensing and process model assessments. *Remote Sensing of Environment*, *175*, 349-358.

Screen, J. A., & Simmonds, I. (2011). Erroneous Arctic temperature trends in the ERA-40 reanalysis: a closer look. *Journal of Climate*, *24*(10), 2620-2627.

Subcommittee, P. (1988). Glossary of permafrost and related ground-ice terms. *Associate Committee on Geotechnical Research, National Research Council of Canada, Ottawa*, *156*.

Raynolds, M. K., Walker, D. A., Ambrosius, K. J., Brown, J., Everett, K. R., Kanevskiy, M., ... & Webber, P. J. (2014). Cumulative geoecological effects of 62 years of infrastructure and climate change in ice-rich permafrost landscapes, Prudhoe Bay Oilfield, Alaska. Global change biology, 20(4), 1211-1224.

Rogov, V. V., Kizyakov, A. I., Leibman, M. O., Perednya, D. D., & Vasiliev, A. A. (2003). Tabular ground ice: cryolithological construction and crystalline structure. In *Proceedings of the Eighth International Conference on Permafrost* (Vol. 2).

Romanovsky, V.E., Smith, S.L., and Christiansen, H.H. (2010b), Permafrost Thermal State in the Polar Northern Hemisphere during the International Polar Year 2007-2009: a Synthesis, *Permafrost and Periglacial Processes*, 21(2), 106-116.

Rowland, J.C., et al. (2010), Arctic Landscapes in Transition: Responses to Thawing Permafrost, *Eos, Transactions American Geophysical Union*, 91(26), 229-230.

Rudy, A. C., Lamoureux, S. F., Treitz, P., & Collingwood, A. (2013). Identifying permafrost slope disturbance using multi-temporal optical satellite images and change detection techniques. *Cold Regions Science and Technology*, *88*, 37-49.

Rudy, A. C., Lamoureux, S. F., Treitz, P., & Van Ewijk, K. Y. (2016). Transferability of regional permafrost disturbance susceptibility modelling using generalized linear and generalized additive models. *Geomorphology*, *264*, 95-108.

Segal, R. A., Lantz, T. C., & Kokelj, S. V. (2016). Acceleration of thaw slump activity in glaciated landscapes of the Western Canadian Arctic. *Environmental Research Letters*, *11*(3), 034025.

Schuler, D.V., Hanssen-Bauer, I. Forland, E.: Long term climate trends of the Yamalo-Nenets AO, *Russia; Norwegian Meteorological Institute* no.8/2010

Schuur, E.A.G., Vogel, J.G., Crummer, K.G., Lee, H., Sickman, J.O., and Osterkamp, T.E. (2009), The effect of permafrost thaw on old carbon release and net carbon exchange from tundra, *Nature*, 459(7246), 556-559.

Schuur, E. A. G., McGuire, A. D., Schädel, C., Grosse, G., Harden, J. W., Hayes, D. J.,Hugelius G., Koven, C.D., Kuhry, P., Lawrence, D., M., Olefeld D., Romanovsky, V.E., Schaefer, K., Turetsky, M.R, Treat, C.C., Vonk,J.E. & Natali, S. M. (2015). Climate change and the permafrost carbon feedback. *Nature*, *520*(7546), 171-179.

Shan, W., Hu, Z., Guo, Y., Zhang, C., Wang, C., Jiang, H., Liu, Y., & Xiao, J. (2015). The impact of climate change on landslides in southeastern of high-latitude permafrost regions of China. *Frontiers in Earth Science*, *3*, 7.

Shur, Y., Hinkel, K. M., & Nelson, F. E. (2005). The transient layer: implications for geocryology and climate-change science. *Permafrost and Periglacial Processes*, *16*(1), 5-17.

Shur, Y. L., & Jorgenson, M. T. (2007). Patterns of permafrost formation and degradation in relation to climate and ecosystems. *Permafrost and Periglacial Processes*, *18*(1), 7-19.

Screen, J. A., & Simmonds, I. (2011). Erroneous Arctic temperature trends in the ERA-40 reanalysis: a closer look. *Journal of Climate*, *24*(10), 2620-2627.

Séjourné, A., Costard, F., Fedorov, A., Gargani, J., Skorve, J., Massé, M., & Mège, D. (2015). Evolution of the banks of thermokarst lakes in Central Yakutia (Central Siberia) due to retrogressive thaw slump activity controlled by insolation. *Geomorphology*, *241*, 31-40.

Shiklomanov, N. I., Streletskiy, D. A., Nelson, F. E., Hollister, R. D., Romanovsky, V. E., Tweedie, C. E., Bockheim, J.G. & Brown, J. (2010). Decadal variations of active-layer thickness in moisture-controlled landscapes, Barrow, Alaska. *Journal of Geophysical Research: Biogeosciences*, *115*(G4).

Streletskiy, D. A., Anisimov, O. A., Vasiliev, A. A., & Whiteman, C. (2015). Permafrost degradation. *Snow and ice-related hazards, risks, and disasters*, 303-344.

Streletskaya, I. D., & Leibman, M. O. (2003, July). Cryogeochemical model of tabular ground ice and cryopegs, Yamal Peninsula, Russia. In *8th International conference on permafrost, Zurich, Switzerland* (pp. 21-25).

Streletskiy, D. A., Anisimov, O. A., Vasiliev, A. A., & Whiteman, C. (2014). Permafrost degradation. *Snow and ice-related hazards, risks, and disasters*, 303-344.

Tarnocai, C., Canadell, J.G., Schuur, E.A.G., Kuhry, P., Mazhitova, G., and Zimov, S. (2009), Soil organic carbon pools in the northern circumpolar permafrost region, *Global Biogeochemical Cycles*, 23(2), GB2023.

Trofaier, A. M., Bartsch, A., Rees, W. G., & Leibman, M. O. (2013). Assessment of spring floods and surface water extent over the Yamalo-Nenets Autonomous District. *Environmental Research Letters*, *8*(4), 045026.

Trofaier, A. M., & Rees, W. G. (2015). The suitability of using ASTER GDEM2 for terrain-based extraction of stream channel networks in a lowland Arctic permafrost catchment. *Fennia-International Journal of Geography*, *193*(1), 66-82.

Tucker, C.J., 1979. Red and photographic infrared linear combinations for monitoring vegetation. *Remote Sensing of Environment* 8 (2), 127–150.

van Everdingen, R. (2005), *Multi-language glossary of permafrost and related ground-ice terms*, edited by N. S. a. I. D. Center, Boulder, CO.

Walker, D. A., Leibman, M. O., Epstein, H. E., Forbes, B. C., Bhatt, U. S., Raynolds, M. K., Comiso , J.A., Gubarkov, A.A., Khomutov, A.V. Jia, G. J.; Koplan, J.O., Kaplan, J.O., Kumpula, T., Kuss, P., Matyshak, G., Moskalenko, N.G., Orekhov, P., Romanovsky, V.E., Ukraientseva, Yu, Q. & Kaarlejärvi, E. (2009). Spatial and temporal patterns of greenness on the Yamal Peninsula, Russia: interactions of ecological and social factors affecting the Arctic normalized difference vegetation index. *Environmental Research Letters*, *4*(4), 045004.

Westermann, S., Østby, T. I., Gisnås, K., Schuler, T. V., & Etzelmüller, B. (2015). A ground temperature map of the North Atlantic permafrost region based on remote sensing and reanalysis data. *The Cryosphere*, *9*(3), 1303-1319.

Wheeler, D., & Wilkinson, C. (2004). From calm to storm: the origins of the Beaufort wind scale. *The Mariner's Mirror*, *90*(2), 187-201.

Widhalm, B., Bartsch, A., Leibman, M., & Khomutov, A. (2017). Active-layer thickness estimation from X-band SAR backscatter intensity. *The Cryosphere*, *11*(1), 483.

Walvoord, M. A., & Kurylyk, B. L. (2016). Hydrologic impacts of thawing permafrost-A review. *Vadose Zone Journal*, *15*(6).

Yang, D., Kane, D., Zhang, Z., Legates, D., & Goodison, B. (2005). Bias corrections of long-term (1973–2004) daily precipitation data over the northern regions. *Geophysical Research Letters*, *32*(19).

Yu, Q., Epstein, H. E., Engstrom, R., Shiklomanov, N., & Strelestskiy, D. (2015). Land cover and land use changes in the oil and gas regions of Northwestern Siberia under changing climatic conditions. *Environmental Research Letters*, *10*(12), 124020.

Zakharova, E. A., Kouraev, A. V., Biancamaria, S., Kolmakova, M. V., Mognard, N. M., Zemtsov, V. A., Kripotin, S.N. & Decharme, B. (2011). Snow cover and spring flood flow in the Northern Part of Western Siberia (the Poluy, Nadym, Pur, and Taz Rivers). *Journal of Hydrometeorology*, *12*(6), 1498-1511.

Zhang, T., Barry, R.G., Knowles, K., Heginbottom, J.A., and Brown, J. (2008), Statistics and characteristics of permafrost and ground-ice distribution in the Northern Hemisphere, *Polar Geography*, 31(1-2), 47-68.

Zhang, Y., Olthof, I., Fraser, R., & Wolfe, S. A. (2014). A new approach to mapping permafrost and change incorporating uncertainties in ground conditions and climate projections. *The Cryosphere*, *8*(6), 2177-2194.

Zeng, H., Jia, G., & Forbes, B. C. (2013). Shifts in Arctic phenology in response to climate and anthropogenic factors as detected from multiple satellite time series. *Environmental Research Letters*, *8*(3), 035036.

Websites

ECMWF (2016) Era Interim data record downloaded from January 2008-December 2015, accessed 23 Aril 2016

http://apps.ecmwf.int/datasets/data/interim-full-daily/levtype=sfc/.

Gazprom (2015) Obskaya – Bovanenkovo railway, accessed September 2016, http://www.gazprom.com/about/production/projects/mega-yamal/obskaya-bovanenkovo/.

Grida(2016), Permafrost extent in the Northern Hemisphere, accessed 15 November 2016, http://www.grida.no/graphicslib/detail/permafrost-extent-in-the-northern hemisphere_1266.

NOAA(2016) Climate Data Online, Climate data record from January 2010–Dezember 2010, NOAA/National Climatic Data Center, accessed September 2016, https://www.ncdc.noaa.gov/cdo-web/.

A Appendix

A-1 R-Scripts

Era Interim

```
source("diagwl.R")
source("BeamFileParser.R")

precipidationData <- parseFile("../data_in/ERA-
 interim/precipitation/precipitation_newdata.txt")

precipidationData$day <- substr(precipidationData$date, 1, 10)

# group data by day and sum day values
daySums <- ddply(
  precipidationData,
  .(day),
  summarize,
  sumPin3=sum(pin_3)*1000 , # add and convert to mm/day
  sumPin1=sum(pin_1)*1000,
  number=length(date)
)

write.csv2(daySums,
 file="../data_out/temperature_precipitation/ERA-
 interim_precipitation_2008_2015_daySums.csv")

# create means per month
monthlyPrecipitationMeans <- ddply(
  daySums,
  .(substr(daySums$day, 1, 7)),
  summarize,
  pin3Mean = sum(sumPin3),
  pin1Mean = sum(sumPin1)
)

write.csv2(monthlyPrecipitationMeans,
 file="../data_out/temperature_precipitation/ERA-
 interim_precipitation_2008_2015_monthlyMeans.csv")

for (y in 2008:2015) {
  data <- parseFile(paste("../data_in/ERA-
 interim/temperature/temperature_", y, ".txt", sep=""))


  # create means / absolute min per month
  monthlyTemperatureMeans <- ddply(
    data,
    .(substr(date, 1, 7)),
    summarise,
    pin3Mean = mean(pin_MaareSale) - 273.15,
    pin1Mean = mean(pin_VaskinyDachi) - 273.15,
    pin3Min = min(pin_MaareSale) - 273.15,
    pin1Min = min(pin_VasknyDAchi) - 273.15
  )

  write.csv2(monthlyTemperatureMeans, file =
 paste(c("../data_out/temperature_precipitation/ERA-
 interim_temperature_monthlyMeans_", y, ".csv"), collapse=''))
```

```
  for (pin in c("pin_Maare Sale", "pin_VaskinyDachi")) {
    precipitation <-
monthlyPrecipitationMeans[substr(monthlyPrecipitationMeans$`subst
r(daySums$day, 1, 7)`,1,4)==as.character(y),][[paste(pin, "Mean",
sep="")]]
    temperature <- monthlyTemperatureMeans[[paste(pin, "Mean",
sep="")]]
    temperatureMin <- monthlyTemperatureMeans[[paste(pin, "Min",
sep="")]]

    diagramData <- rbind(
      precipitation,
      temperature,
      temperature,
      temperatureMin
    )

    write.csv2(diagramData, file =
paste(c("../data_out/temperature_precipitation/ERA-
interim_temperature_precipitation_", y, pin, ".csv"),
collapse=''))

    diagwl(diagramData, est=pin, per=y)
```

Wind rose diagrams

```
library(lubridate)
require(utils)
require(openair)
source("BeamFileParser.R")

calculate_angle <- function(u_val, v_val) {
  d_per_r <- 180 / pi
  # *-1 to get 'from' instead of 'to' wind direction

  dir_geo <- atan2(-1*u_val, -1*v_val) * d_per_r
  # convert negative degrees to 180-360
  if (dir_geo < 0) {
    dir_geo <- 360 + dir_geo
  }
  return(dir_geo)
}

calculate_velocity <- function(u_val, v_val) {
  ws <- sqrt(u_val*u_val + v_val*v_val)
  return(ws)
}

u <- parseFiles("../data_in/ERA-interim/wind/Wind_2008_U.txt",
                "../data_in/ERA-interim/wind/Wind_2009_U.txt",
                "../data_in/ERA-interim/wind/Wind_2010_U.txt",
                "../data_in/ERA-interim/wind/Wind_2011_U.txt",
                "../data_in/ERA-interim/wind/Wind_2012_U.txt",
                "../data_in/ERA-interim/wind/Wind_2013_U.txt",
                "../data_in/ERA-interim/wind/Wind_2014_U.txt",
                "../data_in/ERA-interim/wind/Wind_2015_U.txt")
v <- parseFiles("../data_in/ERA-interim/wind/Wind_2008_V.txt",
                "../data_in/ERA-interim/wind/Wind_2009_V.txt",
                "../data_in/ERA-interim/wind/Wind_2010_V.txt",
```

```
                "../data_in/ERA-interim/wind/Wind_2011_V.txt",
                "../data_in/ERA-interim/wind/Wind_2012_V.txt",
                "../data_in/ERA-interim/wind/Wind_2013_V.txt",
                "../data_in/ERA-interim/wind/Wind_2014_V.txt",
                "../data_in/ERA-interim/wind/Wind_2015_V.txt")

for (pin in c("pin_VaskinyDachi", "pin_MaareSale")) {
  wd <- mapply(calculate_angle, u[[pin]], v[[pin]], SIMPLIFY =
TRUE)
  ws <- mapply(calculate_velocity, u[[pin]], v[[pin]], SIMPLIFY =
TRUE)

  windroseData <- data.frame(date=u$date, wd=wd, ws=ws)

  write.csv2(windroseData,                 file                  =
paste(paste("../data_out/wind/ERA-interim_Wind_2008_2015_",  pin,
sep=""), ".csv", sep=""))

  # edit for summer / winter month
  windroseDataSummer  <-  subset(windroseData,  month(date)  >  6  &
month(date) < 10)
  windRose(windroseDataSummer,  type  =  "year",  breaks  =  c(0,  8,
10.8, 13.9, 17.2), key.header=paste(pin, "summer"))

  # edit for summer / winter month
  windroseDataWinter  <-  subset(windroseData,  month(date)  <  6  |
month(date) > 9)
  windRose(windroseDataWinter,  type  =  "year",  breaks  =  c(0,  8,
10.8, 13.9, 17.2), key.header=paste(pin, "winter"))
```

NOAA - Observed Data

```
source("diagwl.R")

dailyData <- read.csv("../data_in/NOAA/NOAA_daily.webarchive")
monthlyData <- read.csv("../data_in/NOAA/NOAA_monthly.webarchive")

for (year in 2011:2015) {
  dailyDataForYear <- dailyData[substr(dailyData$DATE,1,4) ==
 year,]
  dailyDataForYear$PRCP[dailyDataForYear$PRCP<0] <- 0 # replace <0
 with 0
  monthlyPrecipitation <- tapply(dailyDataForYear$PRCP,
 substr(dailyDataForYear$DATE, 5, 6), sum)

  dailyDataForYear <- dailyData[substr(dailyData$DATE,1,4) == year
 & dailyData$TMAX>(-9000),]
  monthlyTemperatureMaxMean <- tapply(dailyDataForYear$TMAX,
 substr(dailyDataForYear$DATE, 5, 6), mean)

  dailyDataForYear <- dailyData[substr(dailyData$DATE,1,4) == year
 & dailyData$TMIN>(-9000),]
  monthlyTemperatureMinMean <- tapply(dailyDataForYear$TMIN,
 substr(dailyDataForYear$DATE, 5, 6), mean)


  diagramData <- rbind(monthlyPrecipitation,
 monthlyTemperatureMaxMean, monthlyTemperatureMinMean, monthlyMin)

  write.csv2(diagramData, file =
 paste(c("../data_out/temperature_precipitation/NOAA_temperature_p
 recipitation_", year, ".csv"), collapse=''))

  diagwl(diagramData, est="NOAA", per=year)
}
```

A-2 Anthropogenic Disturbances

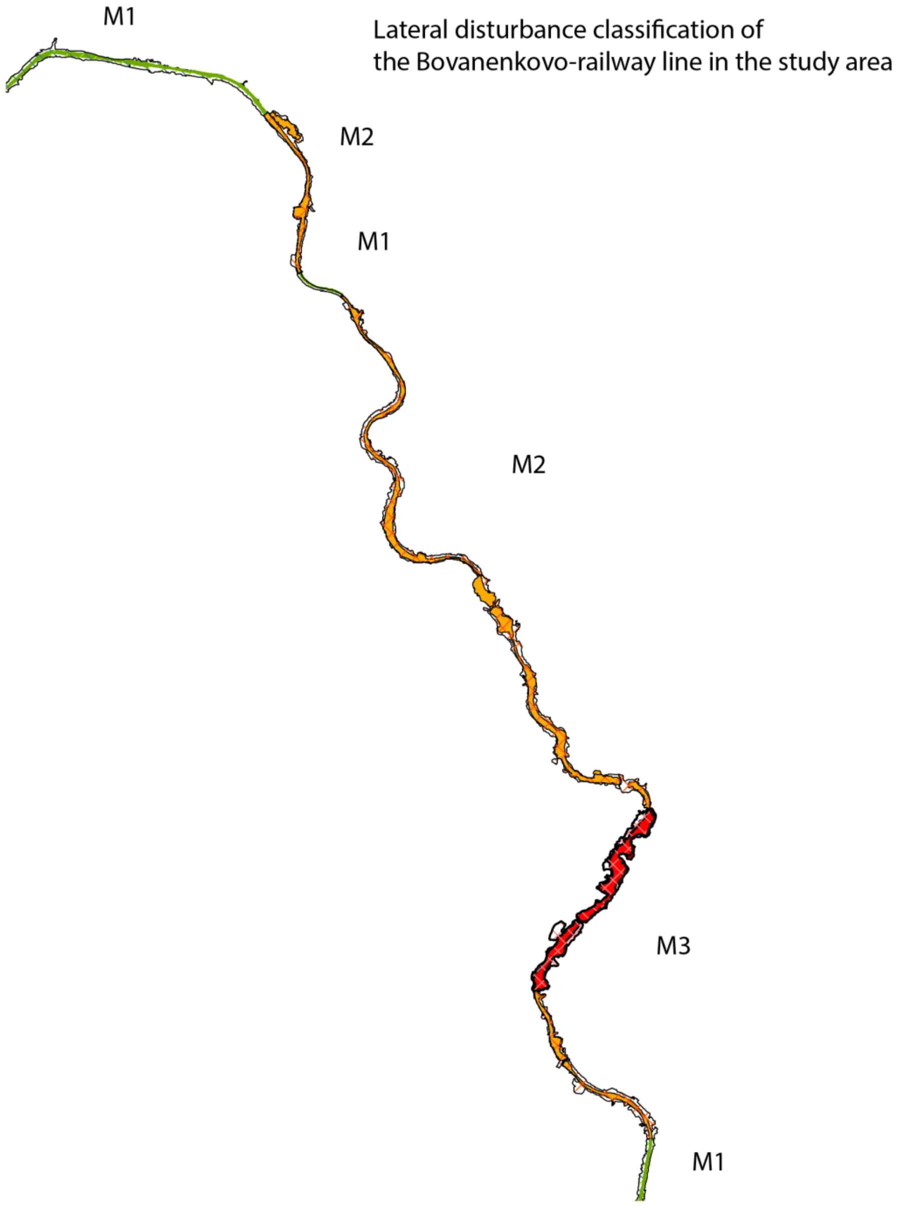

Figure A -1 Illustration of railway disturbance classification

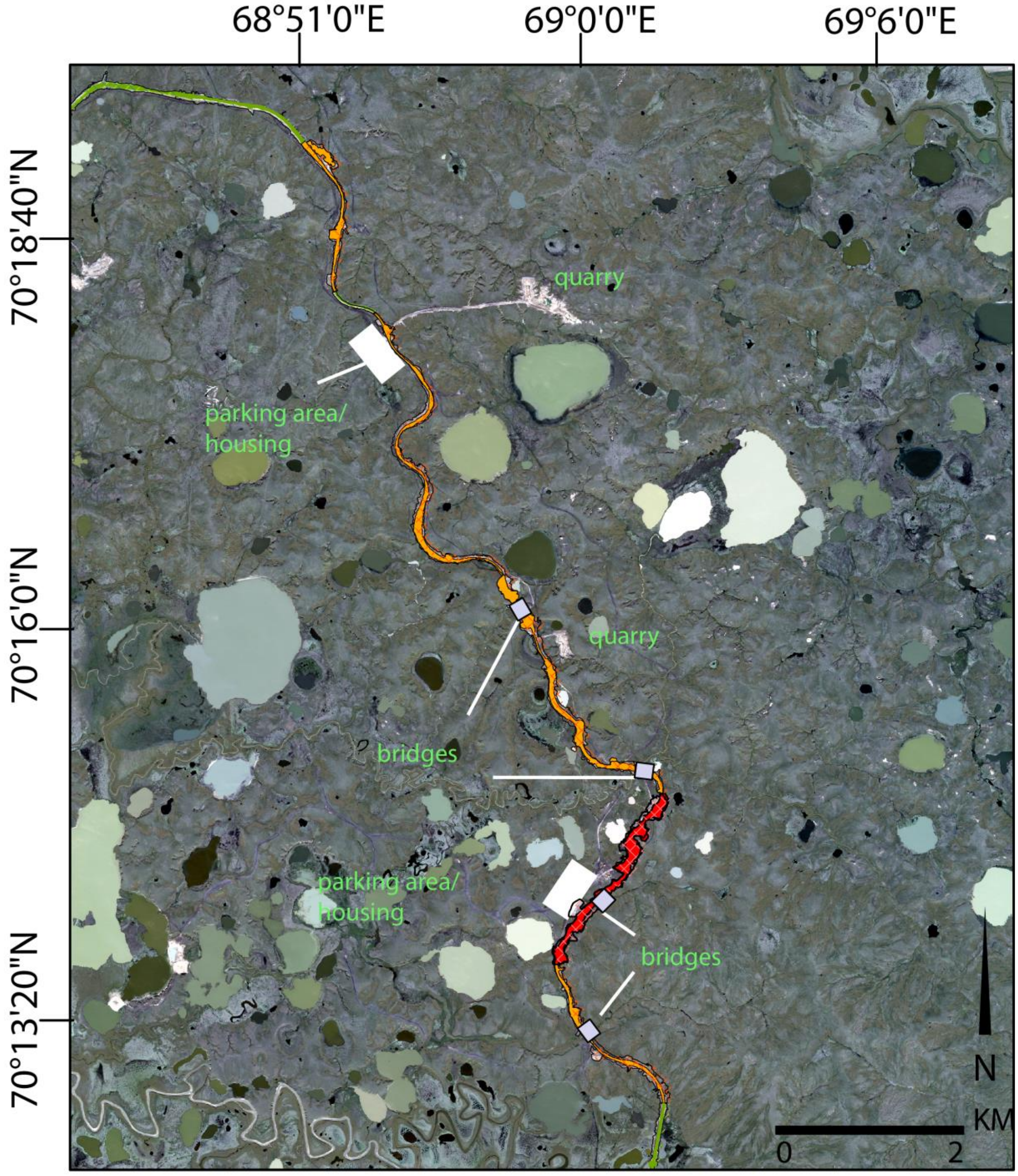

Figure A-2 Construction features of railway line

A-3 ASCAT Metop-A Backscatter Data and SSF

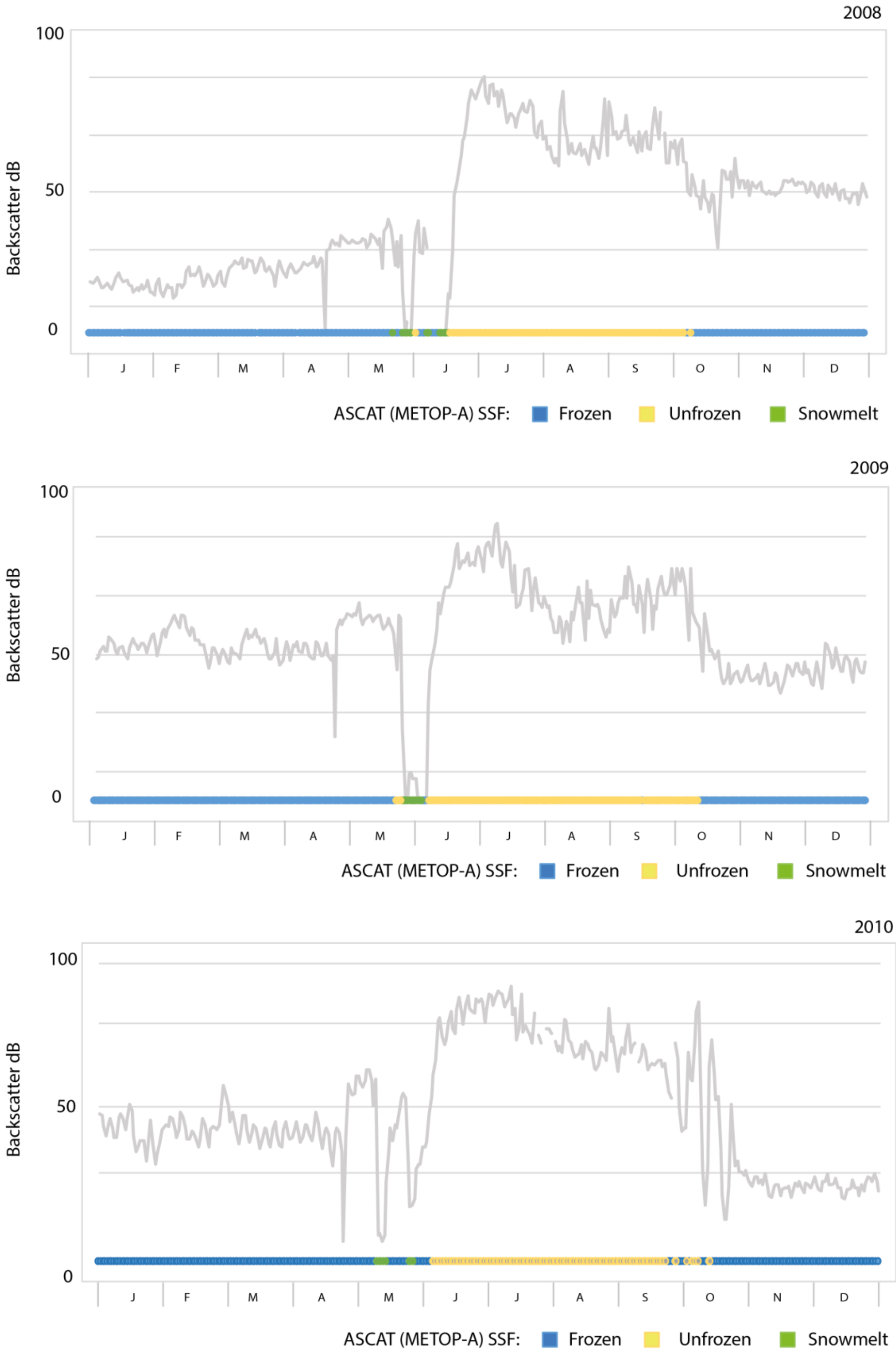

Figure A-3 (1/2) Backscatter and SSF data from ASCAT Metop-A satellite 2008 -2010

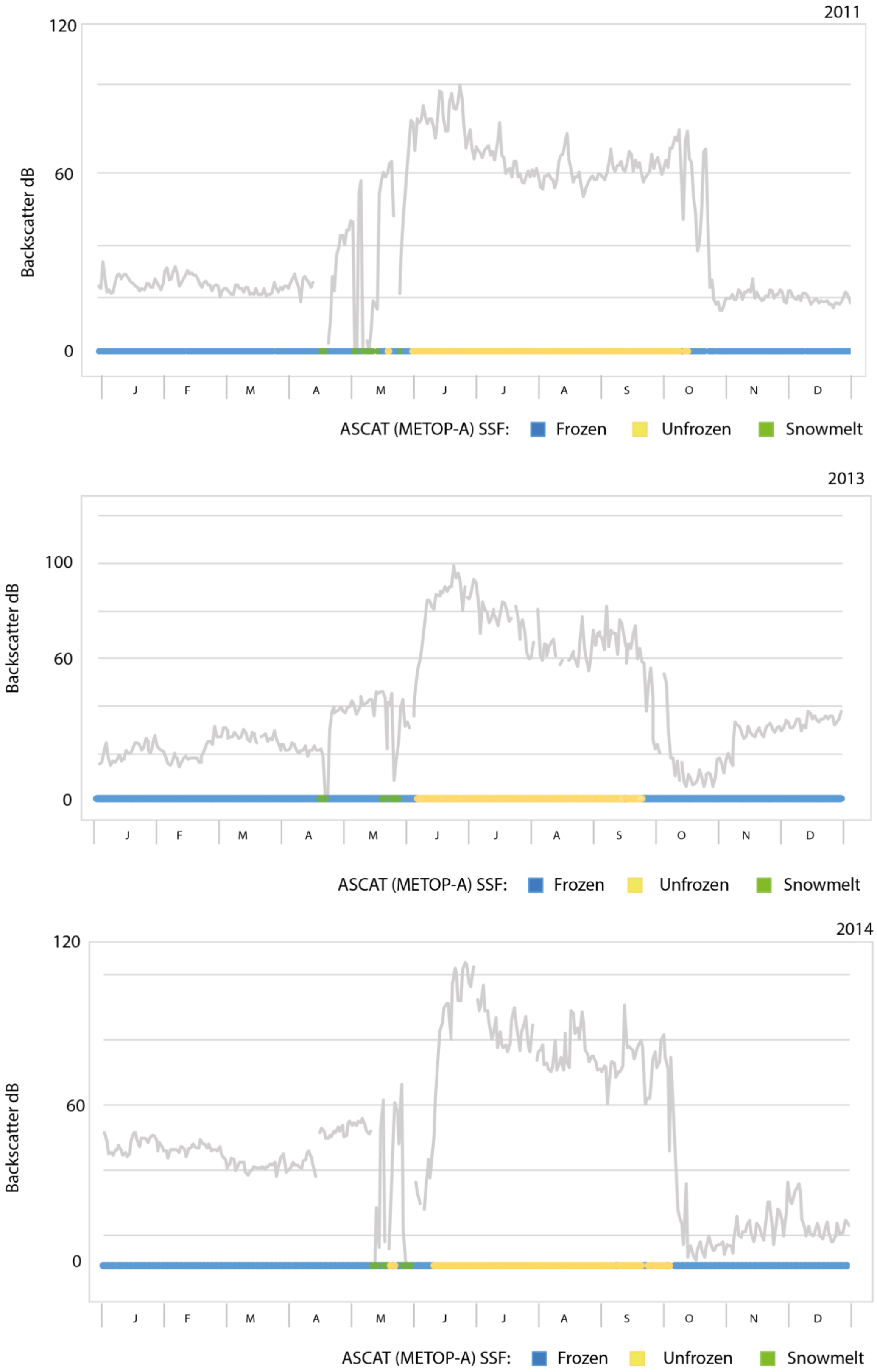

Figure A 3 (2/2) Backscatter and SSF data from ASCAT Metop-A satellite 2008 -2010

Danksagung

Ein großes Dankeschön geht an Anne Morgenstern für die sehr engagierte und hervorragende Betreuung meiner Masterarbeit. Jede Phase dieser Arbeit wurde von ihr intensiv und mit wegweisenden Anmerkungen unterstützt, welche maßgeblich zum Gelingen dieser Arbeit beitrugen.

Birigt Heim möchte ich für ihr Engagement, die Bereitstellung des Arbeitsplatzes und für ihre fachliche Unterstützung herzlich danken.

Bei Birgit und Anne möchte ich mich zudem bedanken, dass Sie es mir ermöglicht haben an der ICOP 2016 teilzunehmen - eine für mich sehr wertvolle und inspirierende Erfahrung.

Ebenfalls möchte ich mich bei Bernhard Diekmann für die Zweitbetreuung meiner Arbeit bedanken.

Bei Yuri möchte ich mich für die Bereitstellung der Daten, die Geländeexpertise und für die humorvolle Atmosphäre im Büro bedanken.

Weiterhin bedanke ich mich bei Annett Bartsch für den wissenschaftlichen Austausch bei der ICOP und für die gestellten Geländebilder und Daten.

Ein besonderer Dank geht an Daniel für die unverzichtbare und geduldige Unterstützung beim Programmieren mit R. Er stand mir stets mit umfassenden Programmierkenntnissen und zusätzlich erstellten R-Rätseln zur Seite.

Danke an Rici und Kristin für einfach alles –ich bin sehr froh, dass ich euch habe.

Ein großer Dank geht auch an Sonya und Annika für das Korrekturlesen und das Interesse an meiner Arbeit.

Meinen größten Dank möchte ich zuletzt meinen Eltern und meiner Oma zum Ausdruck bringen, die mir immer Verständnis entgegenbracht haben und mir alle Wege in meinem Studium offengehalten haben.

Eigenständigkeitserklärung

Hiermit versichere ich, dass ich die vorliegende Arbeit selbständig verfasst und keine anderen als die angegebenen Quellen und Hilfsmittel verwendet habe. Alle von Autoren wörtlich übernommenen Stellen, wie auch sich an die Gedanken anderer Autoren eng anlehnende Ausführungen meiner Arbeit, sind unter Angabe der Quelle kenntlich gemacht. Außerdem versichere ich, dass diese Arbeit in gleicher oder ähnlicher Fassung noch nicht Bestandteil einer Studien- oder Prüfungsleistung war.

Berlin, den 27. April 2017

Caroline Noerling